

Modeling of Thermal Emission from ULX Pulsar Swift J0243.6+6124 with General Relativistic Radiation MHD simulations

AKIHIRO INOUE ¹, KEN OHSUGA ¹, HIROYUKI R. TAKAHASHI ², AND YUTA ASAHINA ¹

¹*Center for Computational Sciences, University of Tsukuba, 1-1-1 Ten-nodai, Tsukuba, Ibaraki 305-8577, Japan*

²*Department of Natural Sciences, Faculty of Arts and Sciences, Komazawa University, Tokyo 154-8525, Japan*

ABSTRACT

We perform general relativistic radiation magnetohydrodynamics (MHD) simulations of super-Eddington accretion flows around a neutron star with a dipole magnetic field for modeling the galactic ultra-luminous X-ray source (ULX) exhibiting X-ray pulsations, Swift J0243.6+6124. Our simulations show the accretion columns near the magnetic poles, the accretion disk outside the magnetosphere, and the outflows from the disk. It is revealed that the effectively optically thick outflows, consistent with the observed thermal emission at $\sim 10^7$ K, are generated if the mass accretion rate is much higher than the Eddington rate \dot{M}_{Edd} and the magnetospheric radius is smaller than the spherization radius. In order to explain the blackbody radius ($\sim 100 - 500$ km) without contradicting the reported spin period (9.8 s) and spin-up rate ($\dot{P} = -2.22 \times 10^{-8} \text{ s s}^{-1}$), the mass accretion rate of $(200 - 1200)\dot{M}_{\text{Edd}}$ is required. Since the thermal emission was detected in two observations with \dot{P} of $-2.22 \times 10^{-8} \text{ s s}^{-1}$ and $-1.75 \times 10^{-8} \text{ s s}^{-1}$ but not in another with $\dot{P} = -6.8 \times 10^{-9} \text{ s s}^{-1}$, the surface magnetic field strength of the neutron star in Swift J0243.6+6124 is estimated to be between 3×10^{11} G and 4×10^{12} G. From this restricted range of magnetic field strength, the accretion rate would be $(200 - 500)\dot{M}_{\text{Edd}}$ when the thermal emission appears and $(60 - 100)\dot{M}_{\text{Edd}}$ when it is not detected. Our results support the hypothesis that the super-Eddington phase in the 2017-2018 giant outburst of Swift J0243.6+6124 is powered by highly super-Eddington accretion flows onto a magnetized neutron star.

1. INTRODUCTION

Ultra-Luminous X-ray sources (ULXs) are bright X-ray compact objects, whose X-ray luminosities exceed the Eddington luminosity for stellar mass black holes $\sim 10^{39} \text{ erg s}^{-1}$, and have been discovered in off-nuclear regions of our galaxy and nearby galaxies (see reviews by Kaaret et al. 2017; Fabrika et al. 2021). Recently, several ULXs have been shown to have coherent pulsations at periods, $\sim 1 - 10$ s (e.g., Bachetti et al. 2014; Fürst et al. 2016; Israel et al. 2017a,b). These objects are called ULX Pulsars (ULXPs). It is widely believed that these pulsations can be observed if the radiation from the vicinity of the neutron star (NS) periodically changes via rotation of the NS. In this case, the ULXP is powered by a super-Eddington accretion onto the magnetized NS since the luminosity of the ULXP exceeds the Eddington luminosity for the NS, L_{Edd} .

The super-Eddington accretion flows around the magnetized NS consist of the accretion disk, the outflows, and the accretion columns. The super-Eddington accretion disk is truncated at a certain radius, called the truncation radius, by the magnetic fields of the NS, provided that the magnetic field strength of the NS is high enough to prevent disk accretion. It is considered that radiatively driven outflows are launched from the super-Eddington accretion disk, which forms on the outside of the truncation radius, since the vertical radiation pressure force is larger than the vertical gravitational force (Shakura & Sunyaev 1973; Poutanen et al. 2007). The gas moves along the magnetic field lines inside the truncation radius. Then, column accretion flows, called the accretion columns, are formed near the magnetic poles of the NS. The radiative luminosity at the base of the accretion columns exceeds the Eddington luminosity (Basko & Sunyaev 1976; Mushtukov et al. 2015; Kawashima et al. 2016). If the magnetic axis is misaligned with the rotation axis of the NS, then the pulsation exceeding the Eddington luminosity can be observed via the precession of the accretion columns (Mushtukov et al. 2018; Inoue et al. 2020). This inflow-outflow structure around

the magnetized NS has been shown by general relativistic radiation magnetohydrodynamics (GR-RMHD) simulations of super-Eddington accretion flows onto a NS with a dipole magnetic field (Takahashi & Ohsuga 2017; Abarca et al. 2021).

Recent observations suggested that outflows exist in ULXs (see e.g., Pinto et al. 2016) and ULXPs (see e.g., Kosec et al. 2018). In the galactic ULXP, Swift J0243.6+6124, the outflows, as well as a relativistic jet (van den Eijnden et al. 2018), were reported (see e.g., Tao et al. 2019; van den Eijnden et al. 2019). Tao et al. (2019) showed that the radiation spectrum of Swift J0243.6+6124, at the peak of the 2017-2018 giant outburst, can be explained by the thermal blackbody at $0.4 - 0.6 \text{ keV} \sim 10^7 \text{ K}$, with a radius of $100 - 500 \text{ km}$ (however, see also Jaisawal et al. 2019). This thermal emission is considered to originate from the optically thick outflows. It is not known whether the outflows appearing in the numerical simulations mentioned above can explain such thermal emission. Although a semi-analytical model was proposed to account for the effects of the outflows (Mushtukov et al. 2019; Chashkina et al. 2019), it remains to be unclear whether such powerful outflows can occur or not.

In this paper, we perform GR-RMHD simulations of super-Eddington accretion flows onto a NS with a dipole magnetic field for modeling of Swift J0243.6+6124. The dependence of the magnetospheric and outflow structure on the surface magnetic field strength at the NS surface B_{NS} and the mass accretion rate \dot{M}_{in} , which is not investigated in previous studies (Takahashi & Ohsuga 2017; Abarca et al. 2021), is reported. It is revealed that the super-Eddington accretion onto the magnetized NS reproduces the thermal emission observed in this object. We also restrict B_{NS} and \dot{M}_{in} based on the condition of the thermal emission. The paper is organized as follows: we will describe the numerical methods in Section 2 and then present the results in Section 3. Section 4 is devoted to the discussion. Finally, we give our conclusion in the final section.

2. NUMERICAL METHODS

In this study, we numerically solve the GR-RMHD equations in Schwarzschild polar coordinates (t, r, θ, ϕ) , assuming axisymmetry with respect to $\theta = 0, \pi$. We use the GR-RMHD simulation code, UWABAMI (Takahashi & Ohsuga 2017). The moment formalism is adopted to describe the radiation field (Thorne 1981). M1 closure is used as the closure relation (Levermore 1984; Kanno et al. 2013; Sadowski et al. 2013). Using the closure, the radiation fields can be updated by solving the 0-th and 1st moment equations of the radiation without solving the radiative transfer equation. Hereafter, Greek suffixes and Latin suffixes represent spacetime components and space components, respectively. The speed of light c and the gravitational constant G are set to 1 unless otherwise noted.

2.1. Basic equations

The basic equations are as follows (see e.g., Takahashi et al. 2018), the mass conservation law,

$$(\rho u^\mu)_{;\mu} = 0, \quad (1)$$

the energy-momentum conservation laws for magnetohydrodynamics (MHD),

$$(T^{\mu\nu})_{;\nu} = G^\mu, \quad (2)$$

the energy-momentum conservation laws for the radiation field,

$$(R^{\mu\nu})_{;\nu} = -G^\mu, \quad (3)$$

the induction equations,

$$\partial_t (\sqrt{-g} B^i) + \partial_j \{ \sqrt{-g} (b^i u^j - b^j u^i) \} = 0, \quad (4)$$

where ρ is the proper mass density, u^μ is the four-velocity of the gas, B^i is the magnetic field vector in the laboratory frame, b^μ is the magnetic four-vector in the fluid frame, and g is the determinant of the metric, $g = \det(g_{\mu\nu})$. The energy momentum tensor of ideal MHD $T^{\mu\nu}$ consists of that of fluid $T_{\text{gas}}^{\mu\nu}$ and electromagnetic field $M^{\mu\nu}$:

$$T_{\text{gas}}^{\mu\nu} = (\rho + e + p_{\text{gas}}) u^\mu u^\nu + p_{\text{gas}} g^{\mu\nu}, \quad (5)$$

$$M^{\mu\nu} = b^2 u^\mu u^\nu + p_{\text{mag}} g^{\mu\nu} - b^\mu b^\nu, \quad (6)$$

where e is the internal energy density, $p_{\text{gas}} = (\Gamma - 1)e$ is the gas pressure ($\Gamma = 5/3$), and $p_{\text{mag}} = b^2/2$ is the magnetic pressure in the fluid frame. The energy momentum tensor of the radiation field in the M1 formalism is given by Sadowski et al. (2013),

$$R^{\mu\nu} = (\bar{E} + p_{\text{rad}}) u_{\text{R}}^\mu u_{\text{R}}^\nu + \frac{1}{3} \bar{E} g^{\mu\nu}. \quad (7)$$

Here, \bar{E} , $p_{\text{rad}} = \bar{E}/3$, and u_{R}^μ are the radiation energy density, the radiation pressure in the radiation rest frame, and the four-velocity of the radiation rest frame, respectively. The radiation four-force G^μ , which describes the interaction between the ideal MHD and radiation field, is defined as

$$G^\mu = -\rho\kappa_{\text{abs}} \left(R^{\mu\alpha} u_\alpha + 4\pi\hat{B}u^\mu \right) - \rho\kappa_{\text{sca}} \left(R^{\mu\alpha} u_\alpha + R^{\alpha\beta} u_\alpha u_\beta u^\mu \right) + G_{\text{comp}}^\mu, \quad (8)$$

where κ_{abs} and κ_{sca} are the opacity for free-free absorption and isotropic electron scattering, respectively:

$$\kappa_{\text{abs}} = 6.4 \times 10^{22} \rho T_e^{-3.5} \quad [\text{cm}^2 \text{ g}^{-1}], \quad (9)$$

$$\kappa_{\text{sca}} = 0.4 \quad [\text{cm}^2 \text{ g}^{-1}]. \quad (10)$$

Here, T_e is the electron temperature. The blackbody intensity is given by $\hat{B} = aT_e^4/4\pi$, where a is the radiation constant. In this study, we consider the thermal comptonization defined as follows (Fragile et al. 2018; Utsumi et al. 2022) :

$$G_{\text{comp}}^\mu = -\kappa_{\text{sca}} \rho \hat{E} \frac{4k(T_e - T_r)}{m_e} u^\mu. \quad (11)$$

Here, \hat{E} is the radiation energy density in the fluid frame, $T_r = (\hat{E}/a)^{1/4}$ is the radiation temperature and m_e is the electron rest mass. We take $T_e = T_g$ for simplicity, where T_g is the gas temperature. The gas temperature can be derived from

$$T_g = \frac{\mu_w m_p p_{\text{gas}}}{\rho k}, \quad (12)$$

where m_p is the proton mass, k is the Boltzmann constant, and $\mu_w = 0.5$ is the mean molecular weight. We consider the mean-field dynamo in our simulations (Sadowski et al. 2015).

2.2. Numerical models

In this study, we take $M_{\text{NS}} = 1.4M_\odot$ and $r_{\text{NS}} = 10$ km, where M_{NS} and r_{NS} are the mass and radius of the NS, and consider the NSs with dipole magnetic fields (Wasserman & Shapiro 1983). The dipole magnetic field strength at the NS surface B_{NS} applied in this study, which is relatively weaker than the typical value observed in the X-ray pulsar, 10^{11-13} G (see Section 4.5), is described in Table 1. The table also reports the maximum gas density of the initial torus ρ_0 , the end time of the simulation t_{end} , the time after which the mass outflow rate is almost constant t_{eq} , and numerical grid points (N_r, N_θ) . The light-crossing time for the gravitational radius of the NS, $r_g = M_{\text{NS}} = 2.1$ km, is denoted by t_g . The computational domain consists of $r = [r_{\text{NS}}, r_{\text{out}}]$, where $r_{\text{out}} = 2100$ km, and $\theta = [0, \pi]$. The size of the radial grid exponentially increases with r , and the size of the polar grid is uniform (Takahashi & Ohsuga 2017). Multipole components of the NS magnetic field are not considered. GR-RMHD simulations considering the multipole components are left as an important future work, although the GR-MHD simulations employing quadrupole fields were recently performed by Das et al. (2022). The rotation of the NSs is ignored since the rotation period of the NSs observed in ULXPs, 1 – 10 s, is much longer than the rotational timescale of the accretion disk, $\sim 10^{-2}$ s, even within $r \sim 100$ km. There remains the possibility that ULX is a millisecond pulsar (Kluźniak & Lasota 2015), which we will discuss later. We assume that the magnetic axis coincides with the rotation axis of the accretion disk. The convergence of the simulation results is confirmed using models B1e10D001, B1e10D001_a, B1e10D001_b, and B1e10D001_c. These models have the same initial parameters except for the resolution.

We initially set the equilibrium torus given by Fishbone & Moncrief (1976), as can be seen in Figure 1, where $(R, z) = (r \sin \theta, r \cos \theta)$. The gas pressure p_{gas} inside the torus is replaced with $p_{\text{gas}} + p_{\text{rad}}$ by assuming a local thermodynamic equilibrium, $T_g = T_r$. The inner edge of the torus and the maximum pressure radius are set to 210 km and 304.5 km, respectively. The poloidal-loop magnetic fields inside the torus are considered in addition to the dipole magnetic field of the NS. The vector potential of this loop magnetic field is proportional to ρ . The embedded loop magnetic field is anti-parallel to the dipole magnetic field at the inner edge of the torus (Romanova et al. 2011;

Table 1. Parameters for different models

Parameter	B_{NS}	ρ_0	t_{end}	t_{eq}	(N_r, N_θ)
Unit	[G]	[g cm $^{-3}$]	[t_g]	[t_g]	
B3e9D001	3.3×10^9	0.01	50000	30000	(592, 412)
B3e9D01_np	3.3×10^9	0.1	50000	40000	(592, 412)
B1e10D001	10^{10}	0.01	50000	30000	(592, 512)
B1e10D002	10^{10}	0.021	50000	30000	(592, 512)
B1e10D004	10^{10}	0.046	50000	35000	(592, 512)
B1e10D01	10^{10}	0.1	50000	35000	(592, 412)
B1e10D1_np	10^{10}	1	50000	40000	(592, 512)
B3e10D001	3.3×10^{10}	0.01	50000	40000	(732, 512)
B3e10D01	3.3×10^{10}	0.1	50000	35000	(732, 512)
B3e10D02	3.3×10^{10}	0.21	50000	40000	(592, 512)
B3e10D04	3.3×10^{10}	0.46	50000	40000	(592, 512)
B3e10D1	3.3×10^{10}	1	50000	40000	(592, 412)
B1e10D001_a	10^{10}	0.01	40000	25000	(732, 512)
B1e10D001_b	10^{10}	0.01	40000	30000	(592, 412)
B1e10D001_c	10^{10}	0.01	40000	30000	(592, 326)

NOTE— B_{NS} , ρ_0 , and (N_r, N_θ) are the surface magnetic field strength of the NS, the maximum gas density of the initial torus, and numerical grid points, respectively. The simulation continues until $t = t_{\text{end}}$. The mass outflow rate is almost constant after $t = t_{\text{eq}}$. The model without accretion columns is denoted by **_np** at the end of the model name.

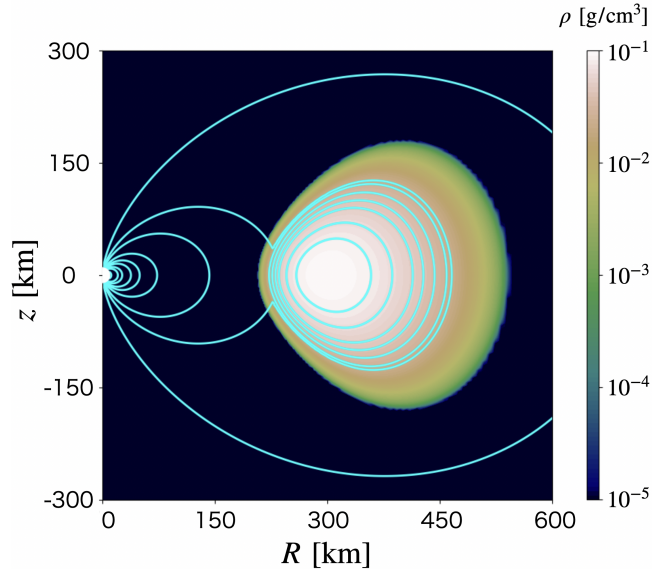


Figure 1. Snapshot of density for initial equilibrium torus in the case of model B1e10D01. Solid lines represent magnetic field lines.

Takahashi & Ohsuga 2017; Parfrey & Tchekhovskoy 2017). We set the maximum $(p_{\text{gas}} + p_{\text{rad}})/p_{\text{mag}}$ to 100 inside the torus. We give a perturbation on $p_{\text{gas}} + p_{\text{rad}}$ by 10% to break an equilibrium state of the torus.

The NS and torus are initially surrounded by relatively hot and low-density corona,

$$\rho = \max \left[\rho_{\text{flr}}, \rho_c \left(\frac{r_{\text{NS}}}{r} \right)^{-5} \right],$$

$$p_{\text{gas}} = \max \left[p_{\text{flr}}, \min \left[\frac{k\rho T_{\text{g,max}}}{\mu_{\text{w}}m_{\text{p}}}, \frac{k\rho_c T_{\text{init}}}{\mu_{\text{w}}m_{\text{p}}} \left(\frac{r_{\text{NS}}}{r} \right)^{-5} \right] \right],$$

where ρ_c is determined by $\sigma_c = B_{\text{NS}}^2/(4\pi\rho_c) = 10^3$, and T_{init} is set to 5×10^{11} K. The floor value of the gas density ρ_{flr} and gas pressure p_{flr} are described in Section 2.3. The radiation energy density of the corona is $\bar{E} = a\bar{T}_{\text{rad}}^4$, where $\bar{T}_{\text{rad}} = 10^5$ K. The velocity of the gas u^i and radiation rest frame u_{R}^i are set to zero in the corona. The present result is not affected by the corona gas which is set initially. This is because these hot gases are blown away by the radiation force from the accretion disk after some time has elapsed since the simulations began.

2.3. Boundary and floor condition

We adopt the outgoing boundary at $r = r_{\text{out}}$, and the reflective boundary at $\theta = 0, \pi$. At the inner boundary, $r = r_{\text{NS}}$, we assume that the boundary, at which the gas can be swallowed by the NS but the energy can not be swallowed by the NS (Ohsuga 2007). At inner ghost cells, ρ , p_{gas} , and \bar{E} are the free boundary, and u^i and u_{R}^i are set to zero. For the magnetic field, the radial component is fixed to be the dipole field (Wasserman & Shapiro 1983), while the tangential component is set according to the free boundary condition (Parfrey & Tchekhovskoy 2017; Abarca et al. 2021). The numerical flux in mass conservation law, energy conservation law for MHD, and energy conservation law for the radiation field are zero at the NS surface. The numerical flux of the induction equation is also set to zero at the NS surface to satisfy the ideal MHD condition. We also impose the following condition on the gas density and pressure at the NS surface:

$$\rho(t) = \min [\rho_*(t), \rho(t=0)], \quad (13)$$

$$p_{\text{gas}}(t) = \frac{k\rho(t)T_{\text{g},*}(t)}{\mu m_{\text{p}}}, \quad (14)$$

where ρ_* and $T_{\text{g},*}$ are the gas density and gas temperature calculated from the conservative variables, respectively. In this case, the gas density is set to initial value by keeping the gas temperature constant at the NS surface. The amount of reduced kinetic and thermal energy densities by applying (13) and (14) is added to the radiation energy density R_t^t . Here, the kinetic and thermal energy densities are defined as follows:

$$U_{\text{kinetic}} = \rho u^t (u_t - \sqrt{-g_{tt}}), \quad (15)$$

$$U_{\text{thermal}} = (e + p_{\text{gas}})u^t u_t + p_{\text{gas}}g_t^t. \quad (16)$$

The mass reduced by the treatment of (13) is considered to be swallowed by the NSs.

We impose a floor condition on ρ and p_{gas} to solve the GR-RMHD equations stably:

$$\rho_{\text{flr}} = \max \left[\frac{b^2}{\sigma_{\text{max}}}, 10^{-4}\rho_0 \left(\frac{r}{r_{\text{g}}} \right)^{-1.5} \right], \quad (17)$$

$$p_{\text{flr}} = 10^{-6}(\Gamma - 1)\rho_0 \left(\frac{r}{r_{\text{g}}} \right)^{-2.5}, \quad (18)$$

where σ_{max} is set to 10^3 . The upper and lower limit of the gas temperature are set to 5×10^{11} K and 5×10^5 K, respectively.

The gas density should be low near $\theta = 0, \pi$ because the strong magnetic pressure and tension due to the open poloidal magnetic field lines inhibit the mass flow toward the rotation axis in the very vicinity of the rotation axis. In the numerical simulation, however, the gas reaches the region of $\theta = 0, \pi$ due to the numerical diffusion. Then, the unphysical mass outflow driven by the radiation force is formed close to the polar axis. We decided to ignore the gas-radiation interaction to avoid this problem in this region. Practically, we set the absorption and scattering opacity to zero at $\sigma > \sigma_{\text{rad}}$, where $\sigma = b^2/\rho$ is the magnetization. In this study, we set $\sigma_{\text{rad}} = 10$ in all models. This value is set so that the opacity near the rotation axis is zero while the radiation from the dense accretion flows at the NS surface can be solved.

3. RESULTS

In all models, the initial torus deviates from the equilibrium state due to the magnetorotational instability (MRI) caused by the differential rotation in the torus after the simulation starts. The angular momentum of the gas is

transported outward, and then the accretion disk is formed around the equatorial plane ($z = 0$ plane). The radiatively driven outflows are launched from the accretion disk. The accretion disk in models B3e9D001, B1e10D001, B1e10D002, B1e10D004, B1e10D01, B3e10D001, B3e10D01, B3e10D02, B3e10D04 and B3e10D1 is truncated before it reaches to the NS surface. Then, the accreting gas moves along magnetic field lines, and column accretion flows (accretion columns) are formed near the poles of the NS. On the other hand, the accretion disk in models B3e9D01_np and B1e10D1_np directly connects to the NS surface without being truncated.

3.1. Quasi-steady state structure

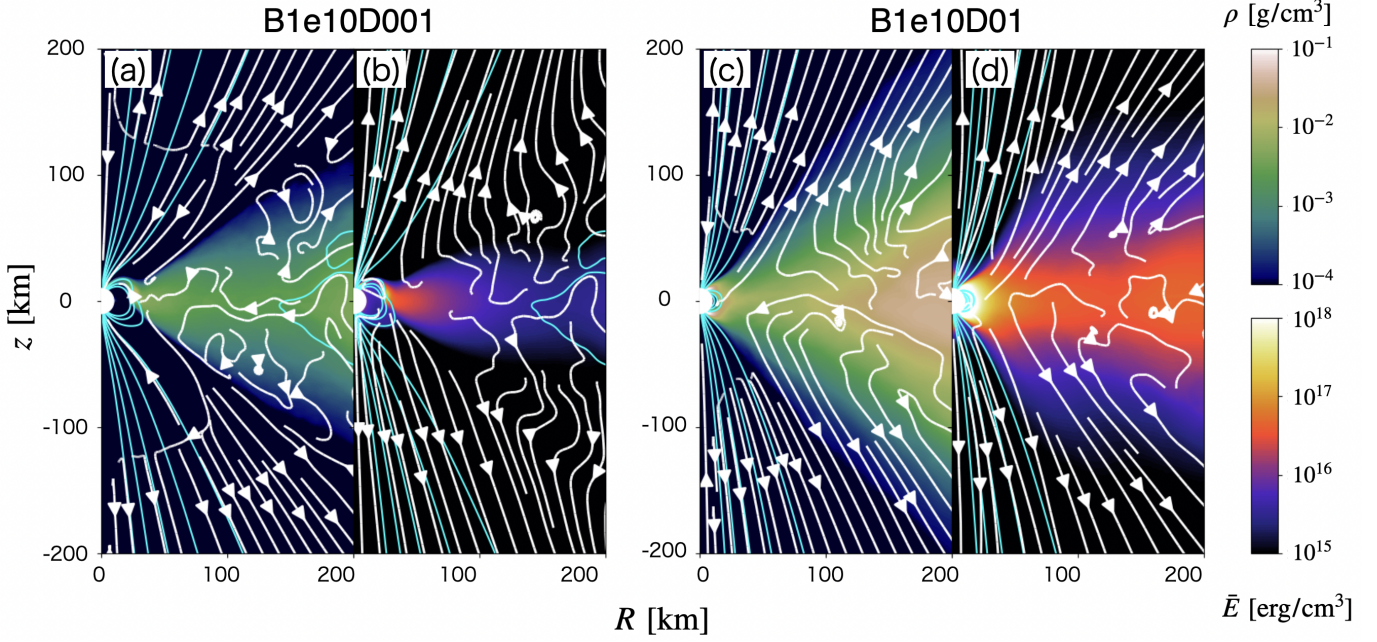


Figure 2. Here, we show the time-averaged quasi-steady structure of super-Eddington accretion flows around the magnetized NS for models B1e10D001 and B1e10D01. Panels (a) and (c): Plot of density profile along with streamlines. Panels (b) and (d): Colors show radiation energy density in the radiation rest frame and streamlines indicate the radiative flux. Cyan lines are magnetic field lines.

We use the numerical data from period t_{eq} to t_{end} shown in Table 1 for investigating a quasi-steady structure in the present work, since the flows become quasi-steady and the mass outflow rate is almost constant after t_{eq} . Firstly, we introduce the quasi-steady structure of the accretion flows and outflows around the magnetized NS. Figure 2 shows the time-averaged overview of models B1e10D001 (left) and B1e10D01 (right) in the quasi-steady state. Colors represent ρ in panels (a) and (c), and \bar{E} in panels (b) and (d). The white region with $r < 10$ km is the NS, and its center is located at the origin, $(R, z) = (0, 0)$. The magnetic field lines are shown by cyan solid lines. We find that the accretion disk is formed near the equatorial plane at $20 \text{ km} \lesssim R \lesssim 200 \text{ km}$ (the green region in panels (a) and (c)). In panels (b) and (d), it is clear that \bar{E} is large in the accretion disk. The accretion column is formed near the NS magnetic poles, $r \lesssim 20 \text{ km}$, the details of which are described in Figure 3. Streamlines follow the poloidal velocity vectors in panels (a) and (c). It can be seen that the outflows are emanated from the disk toward the low-density region. In addition, turbulent motions exist inside the accretion disk. The radiative flux is represented by streamlines in panels (b) and (d). We can see that the outward radiative flux from the accretion disk appears. The accretion disk, the outflows, and the outward radiative flux from the accretion disk are common to all models. Both ρ and \bar{E} in the accretion disk tend to increase as ρ_0 becomes large. Actually, both of ρ and \bar{E} in model B1e10D01 ($\rho_0 = 0.1 \text{ g cm}^{-3}$) are an order of magnitude higher than those in model B1e10D001 ($\rho_0 = 0.01 \text{ g cm}^{-3}$).

We can see that the gas accretes onto the NS around the pole outside the accretion column ($r \lesssim 100 \text{ km}$ and $\theta \lesssim 40^\circ$, $140^\circ \lesssim \theta$ in panel (a)). This is because the interaction between the gas and radiation is artificially switched off at the high- σ region ($\sigma > \sigma_{\text{rad}}$) in our simulation to maintain numerical stability. The radiation force does not work around

the polar axis and the gas falls down to the NS. We note that the density in this region is too small to contribute to the mass accretion rate, and the effects on the overall structure are negligibly small.

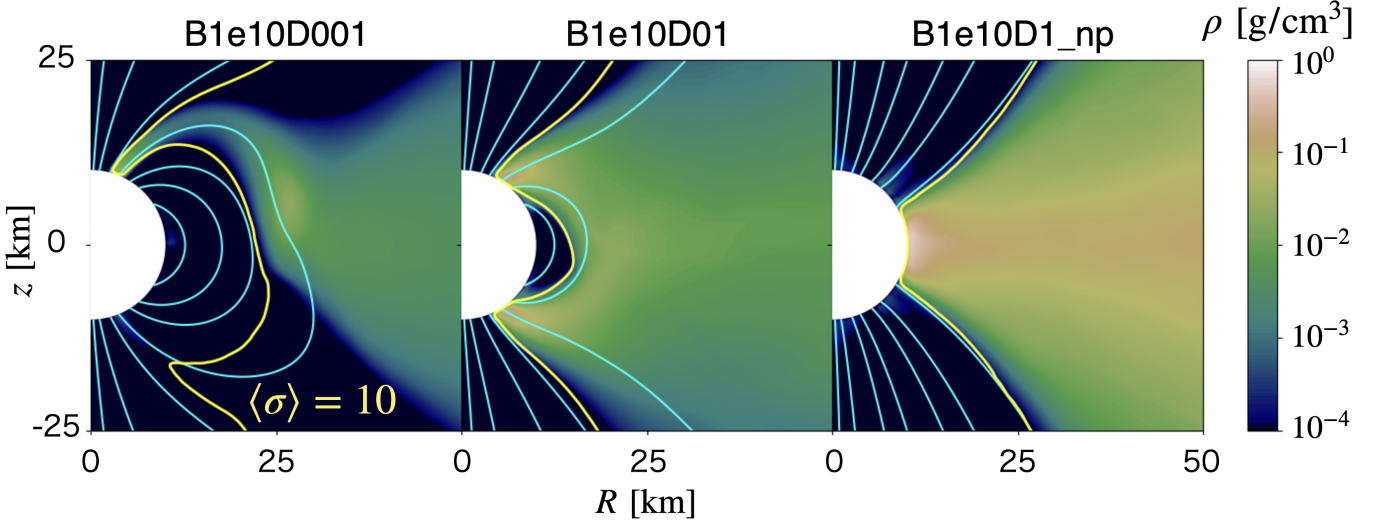


Figure 3. The dependence of accretion flows on the maximum gas density of the initial torus ρ_0 . Colors shows gas density. Yellow lines represents $\langle\sigma\rangle = 10$, where $\langle\sigma\rangle$ is the time-averaged magnetization. Cyan lines are magnetic field lines.

Next, we explain the dependence of the magnetospheric structure on ρ_0 . Colors in Figure 3 show ρ , and magnetic field lines are represented by cyan lines. We take models B1e10D001, B1e10D01, and B1e10D1_np. We plot the time-averaged magnetization, $\langle\sigma\rangle = \langle b^2 \rangle / \langle \rho \rangle = 10$, by yellow contours. Here, the angle brackets denote the time-averaged value. The magnetization $\langle\sigma\rangle$ on the high-density side of the yellow line is less than 10. In the left panel (model B1e10D001), the high-density accretion column, around $(R, z) = (5\text{km}, 12\text{km})$, is formed (one-side accretion). Although not shown in Figure 3, the same is true of models B3e9D001, B1e10D002, B3e10D001, B3e10D01, and B3e10D02. In the middle panel (model B1e10D01), the accretion columns are formed at $(R, z) = (6\text{km}, \pm 10\text{km})$, which is true of models B1e10D004, B3e10D04, and B3e10D1. At the truncation radius, which is the radius of the inner edge of the accretion disk, the gas begins to move away from the equatorial plane toward the NS poles. The truncation radius is $R \sim 25$ km in model B1e10D001 and $R \sim 13$ km in model B1e10D01, and approximately corresponds to the position where $\langle\sigma\rangle = 10$ at the equatorial plane. The density inside this radius is less than 1% of the density of the disk, except inside the accretion column. Also, the truncation radius is roughly comparable to the magnetospheric radius, r_M , ~ 27 km for model B1e10D001 and ~ 13 km for model B1e10D01. In the present work, r_M is defined as the maximum radius of the region, where $\langle\beta\rangle_{u_\phi} < 1$, inside the maximum pressure radius of the initial torus, 304.5 km. Here, $\langle\beta\rangle_{u_\phi}$ is u_ϕ -weighted plasma beta,

$$\langle\beta\rangle_{u_\phi} = \frac{1}{\int_0^\pi \langle u_\phi \rangle \sqrt{g_{\theta\theta}} d\theta} \int_0^\pi \frac{\langle p_{\text{gas}} \rangle + \langle p_{\text{rad}} \rangle}{\langle p_{\text{mag}} \rangle} \langle u_\phi \rangle \sqrt{g_{\theta\theta}} d\theta. \quad (19)$$

Although p_{rad} is the radiation pressure in the radiation rest frame, it is approximately equal to the radiation pressure in the fluid frame since the MHD and radiation field inside the accretion disk are in local thermal equilibrium, and therefore the radiation rest frame coincides with the fluid frame. We note that the gas pressure is negligible in the super-Eddington accretion disk (Takahashi & Ohsuga 2017), so that $p_{\text{mag}} \sim p_{\text{rad}}$ at $\langle\beta\rangle_{u_\phi} = 1$. The coincidence between the truncation radius and r_M indicates that the truncation radius is determined by the balance between p_{mag} and p_{rad} . As can be seen from the left and middle panels in Figure 3, the truncation radius decreases as ρ_0 increases.

In model B1e10D1_np, since the radiation pressure of the accretion disk is larger than the magnetic pressure of the dipole field even at the NS surface, the accretion disk reaches the NS surface without being truncated and no accretion column is formed. In this case, the region where $\langle\beta\rangle_{u_\phi} > 1$ reaches the NS surface, and r_M can not be determined. Although not shown in this figure, accretion columns are not formed in model B3e9D01_np for the same reason. Based on the hypothesis that the radiation from the accretion column is the origin of the X-ray pulse, models B3e9D01_np

Model	$\langle \dot{M}_{\text{in}}(r = 11 \text{ km}) \rangle$	$\langle \dot{M}_{\text{out}}(r_{\text{out}}) \rangle$	$\langle L_{\text{rad}}(r_{\text{out}}) \rangle$	$\langle L_{\text{kin}}(r_{\text{out}}) \rangle$	T_{bb}	r_{bb}
	$[\dot{M}_{\text{Edd}}]$	$[\dot{M}_{\text{Edd}}]$	$[L_{\text{Edd}}]$	$[L_{\text{Edd}}]$	$[10^7 \text{ K}]$	$[\text{km}]$
B3e9D001	32	36	3.0	0.15	0.72	57
B3e9D01_np	220	2700	130	47	0.63	230
B1e10D001	54	74	4.1	0.34	0.71	58
B1e10D002	110	110	9.5	1.0	0.73	65
B1e10D004	160	730	21	7.1	0.66	130
B1e10D01	500	2600	42	36	0.66	240
B1e10D1_np	4700	23000	500	410	0.50	1100
B3e10D001	98	170	5.5	0.89	0.75	50
B3e10D01	720	2900	140	56	0.69	270
B3e10D02	650	4600	150	37	0.63	250
B3e10D04	1500	13000	320	210	0.59	660
B3e10D1	2300	28000	490	460	0.55	1300

Table 2. Time-averaged value for the mass accretion rate, mass outflow rate, radiative luminosity, and kinetic luminosity. The mass accretion rate is measured at $r = 11 \text{ km}$, and the others are calculated at $r = r_{\text{out}}$.

and B1e10D1_np are inappropriate for explaining ULXPs. Incidentally, the reason why the one-side accretion occurs in model B1e10D001 is described in Section 4.4.

Table 2 lists the time-averaged value of the mass accretion rate \dot{M}_{in} at $r = 11 \text{ km}$, mass outflow rate \dot{M}_{out} at $r = r_{\text{out}}$, radiative luminosity L_{rad} at $r = r_{\text{out}}$, and kinetic luminosity L_{kin} at $r = r_{\text{out}}$ of each model. The Eddington mass accretion rate is denoted by $\dot{M}_{\text{Edd}} = L_{\text{Edd}}/c^2$. The mass accretion rate and outflow rate are defined as

$$\dot{M}_{\text{in}}(r) = - \int \min[\rho u^r, 0] \sqrt{-g} d\theta d\phi, \quad (20)$$

$$\dot{M}_{\text{out}}(r) = \int \max[\rho u^r, 0] \sqrt{-g} d\theta d\phi. \quad (21)$$

The radiative and kinetic luminosity can be calculated using following formula (Sadowski et al. 2016):

$$L_{\text{rad}}(r) = - \int \min[R_t^r, 0] \sqrt{-g} d\theta d\phi, \quad (22)$$

$$L_{\text{kin}}(r) = - \int \min[\rho u^r (u_t + \sqrt{-g_{tt}}), 0] \sqrt{-g} d\theta d\phi. \quad (23)$$

As can be seen from this table, \dot{M}_{in} , \dot{M}_{out} , L_{rad} and L_{kin} tend to be large as ρ_0 increases. We also find that $L_{\text{kin}}/L_{\text{rad}}$ tends to be large as \dot{M}_{in} increases. Indeed, the mass accretion rate is $54\dot{M}_{\text{Edd}}$ and $L_{\text{kin}}/L_{\text{rad}} \sim 0.083$ in the case of model B1e10D001, mass accretion rate is $500\dot{M}_{\text{Edd}}$ and $L_{\text{kin}}/L_{\text{rad}} \sim 0.86$ in the case of model B1e10D01, and mass accretion rate is $4700\dot{M}_{\text{in}}$ and $L_{\text{kin}}/L_{\text{rad}} \sim 1.2$ in the case of model B1e10D1_np. That is, the kinetic luminosity is comparable to the radiation luminosity for the model with high mass accretion rate. These trends are also reported in non-relativistic radiation hydrodynamics simulation (Ohsuga 2007).

Figure 4 shows r_{M} and the time derivative of the NS rotation period (spin-up rate) \dot{P} estimated using our numerical models as a function of the mass accretion rate. Points in Figure 4 (a) indicate the resulting r_{M} for $B_{\text{NS}} = 3.3 \times 10^9 \text{ G}$ (red), 10^{10} G (blue), and $3.3 \times 10^{10} \text{ G}$ (black), in which all models have accretion columns. The magnetospheric radius r_{M} decreases with increasing \dot{M}_{in} and increases with increasing B_{NS} . Dashed lines indicate the analytical solution for r_{M} , which can be calculated assuming that the magnetic pressure of the dipole field balances with the radiation pressure of the accretion disk (Takahashi & Ohsuga 2017, see also Appendix B for detail):

$$r_{\text{M}} \sim 2.0 \times 10^6 \text{ [cm]}$$

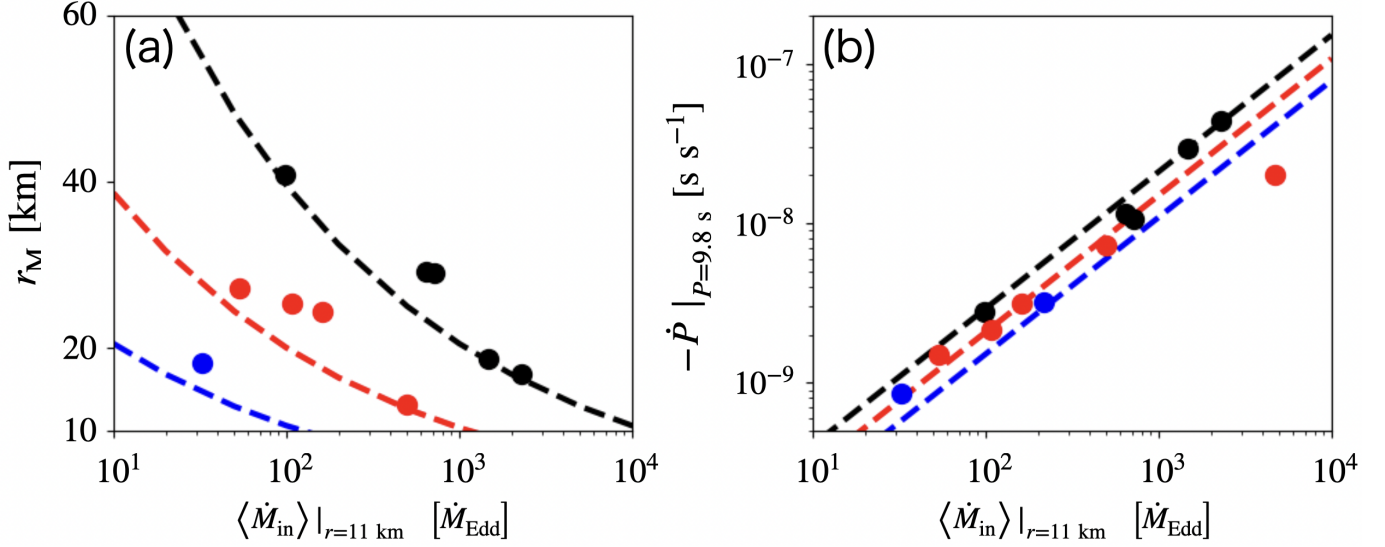


Figure 4. Panel (a): The relations between r_M and the mass accretion rate at the NS surface with different surface magnetic field strengths, $B_{\text{NS}} = 3.3 \times 10^9 \text{ G}$ (red), 10^{10} G (blue), and $3.3 \times 10^{10} \text{ G}$ (black). Dashed lines show the analytical model of r_M (Takahashi & Ohsuga 2017). Panel (b): \dot{P} as a function of the mass accretion rate at the NS surface with different surface magnetic field strengths. Dashed lines show the analytical model of \dot{P} (Takahashi & Ohsuga 2017). Parameters for the analytical model : $M_{\text{NS}} = 1.4M_{\odot}$, $r_{\text{NS}} = 10 \text{ km}$ and $\alpha = 0.1$.

$$\begin{aligned} & \times \left(\frac{\alpha}{0.1} \right)^{2/7} \left(\frac{\dot{M}_{\text{in}}}{10^2 \dot{M}_{\text{Edd}}} \right)^{-2/7} \left(\frac{B_{\text{NS}}}{10^{10} \text{ G}} \right)^{4/7} \\ & \times \left(\frac{M_{\text{NS}}}{1.4M_{\odot}} \right)^{-3/7} \left(\frac{r_{\text{NS}}}{10 \text{ km}} \right)^{12/7}, \end{aligned} \quad (24)$$

where α is the viscous parameter (Shakura & Sunyaev 1973) and we take $\alpha = 0.1$. We can find that the resulting r_M is consistent with the analytical one. We note that the results of models B1e10D1_np and B3e9D01_np are not plotted since r_M is not determined in these models as mentioned above.

We estimate \dot{P} as follows,

$$\dot{P} = \frac{\langle \dot{L} \rangle}{M_{\text{NS}} l_{\text{NS}}} P, \quad (25)$$

$$\dot{L} = \int M_{\phi}^r \sqrt{-g} d\theta d\phi. \quad (26)$$

(Shapiro & Teukolsky 1986; Takahashi & Ohsuga 2017). Here, $l_{\text{NS}} = 2\pi r_{\text{NS}}^2 / P$ and P are the specific angular momentum and rotation period of the NS, respectively. For numerical estimation, we assume $P = 9.8 \text{ s}$, which corresponds to that observed in Swift J0243.6+6124. Figure 4 (b) shows that \dot{P} is in the range from $-10^{-9} \text{ s s}^{-1}$ to $-10^{-7} \text{ s s}^{-1}$, which is not inconsistent with the observed value of Swift J0243.6+6124, $\dot{P} \sim -10^{-8} \text{ s s}^{-1}$ (see Section 3.3 for detail). It is also clearly seen that the larger \dot{M}_{in} and higher B_{NS} leads to large \dot{P} . Dashed lines indicate the analytical solution for \dot{P} , which can be calculated assuming that the Keplerian angular momentum at r_M is transported to the NS without dissipation (Takahashi & Ohsuga 2017, see also Appendix B):

$$\begin{aligned} & \dot{P} \sim -2.2 \times 10^{-9} [\text{s} \cdot \text{s}^{-1}] \\ & \times \left(\frac{\alpha}{0.1} \right)^{1/7} \left(\frac{\dot{M}_{\text{in}}}{10^2 \dot{M}_{\text{Edd}}} \right)^{6/7} \left(\frac{B_{\text{NS}}}{10^{10} \text{ G}} \right)^{2/7} \\ & \times \left(\frac{M_{\text{NS}}}{1.4M_{\odot}} \right)^{2/7} \left(\frac{r_{\text{NS}}}{10 \text{ km}} \right)^{-8/7} \left(\frac{P}{10 \text{ s}} \right)^2. \end{aligned} \quad (27)$$

The resulting \dot{P} is roughly comparable to the analytical one.

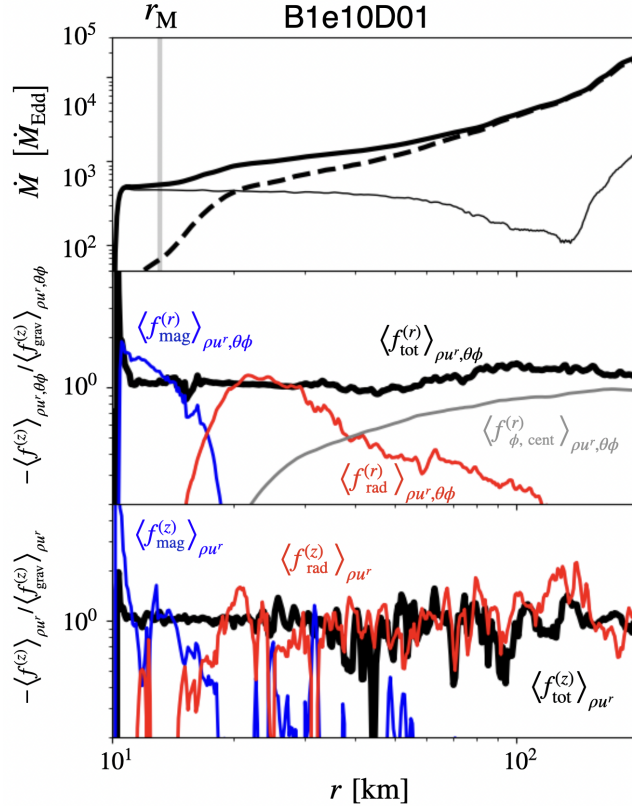


Figure 5. Top: time-averaged radial profiles of the mass accretion rate (thick solid lines), mass outflow rate (dashed lines), and net flow rate (thin solid lines). The vertical line is the position of the magnetospheric radius. Middle: time and shell-averaged mass flux weighted radial forces normalized by the gravitational force. Bottom: time-averaged mass flux weighted vertical forces divided by the vertical gravitational force at $\theta = \pi/2 - \Theta_H$.

3.2. Powerful outflows

In Figure 5, we show that powerful outflows are launched from the super-Eddington accretion disk and are driven by radiation and centrifugal forces. The top panel in Figure 5 shows time-averaged \dot{M}_{in} (thick solid line), \dot{M}_{out} (dashed line), and net flow rate $\dot{M}_{\text{net}} = \dot{M}_{\text{in}} - \dot{M}_{\text{out}}$ (thin solid line) as a function of r in the case of model B1e10D01. The position of r_M in this model is represented by a vertical line. This panel indicates that outflows mainly originate from the accretion disk. This is clearly understood from the fact that \dot{M}_{out} increases significantly with increasing r , and \dot{M}_{out} for $r < r_M$ is much smaller than that for $r > r_M$. The mass accretion rate \dot{M}_{in} decreases with decreasing r due to efficient mass ejection from the accretion disk. The mass outflow rate \dot{M}_{out} is much smaller than the mass accretion rate at $r < r_M$, and we find $\dot{M}_{\text{net}} \sim \dot{M}_{\text{in}} \gg \dot{M}_{\text{out}}$ inside the magnetosphere.

Next, we investigate the radial profile of forces acting on fluid elements. The steady-state axisymmetric equations of motion in the r - and θ -direction in the static observer frame are,

$$f_{\text{grav}}^{(r)} + f_{\text{thermal}}^{(r)} + f_{\theta, \text{cent}}^{(r)} + f_{\phi, \text{cent}}^{(r)} + f_{\text{rad}}^{(r)} + f_{\text{mag}}^{(r)} + f_{\text{adv}}^{(r)} = 0, \quad (28)$$

$$f_{\text{inertial}}^{(\theta)} + f_{\text{thermal}}^{(\theta)} + f_{\phi, \text{cent}}^{(\theta)} + f_{\text{rad}}^{(\theta)} + f_{\text{mag}}^{(\theta)} + f_{\text{adv}}^{(\theta)} = 0, \quad (29)$$

where superscript (r) and (θ) denote the r - and θ -component of the vectors in the static observer frame. The forces acting on fluid elements consist of the gravitational force f_{grav} , thermal force f_{thermal} , radiation force f_{rad} , Lorentz force f_{mag} , centrifugal force f_{cent} , inertial force f_{inertial} , and advection force f_{adv} . The centrifugal force is divided into two components, $f_{\theta, \text{cent}}$ and $f_{\phi, \text{cent}}$, which are caused by the polar (θ -) and azimuthal (ϕ -) motions, respectively (see Appendix C for detail). We define the total force f_{tot} as the sum of all forces without f_{grav} , and therefore $-f_{\text{tot}}^{(r)}/f_{\text{grav}}^{(r)} = 1$ holds.

The middle panel in Figure 5 shows time and shell-averaged mass flux weighted radial forces normalized by the gravitational force as a function of r , which can be calculated as follows:

$$\langle f^{(r)} \rangle_{\rho u^r, \theta \phi} = \frac{1}{\langle \dot{M}_{\text{out}}(r) \rangle} \left\langle \int f^{(r)} \max[\rho u^r, 0] \sqrt{-g} d\theta d\phi \right\rangle. \quad (30)$$

The bottom panel in Figure 5 shows time-averaged mass flux weighted z -component of the forces normalized by the vertical gravitational force,

$$\langle f^{(z)} \rangle_{\rho u^r} = \frac{\langle \max[\rho u^r, 0] f^{(z)} \rangle}{\langle \max[\rho u^r, 0] \rangle}, \quad (31)$$

$$f^{(z)} = f^{(r)} \cos \theta - f^{(\theta)} \sin \theta, \quad (32)$$

at the disk surface. The polar angle of the disk surface is defined as $\theta = \pi/2 - \Theta_{\text{H}}$, where

$$\Theta_{\text{H}} = \left\langle \sqrt{\frac{\int \rho (\pi/2 - \theta)^2 \sqrt{g_{\theta\theta}} d\theta}{\int \rho \sqrt{g_{\theta\theta}} d\theta}} \right\rangle. \quad (33)$$

It is clear that the outflows are mainly driven by the radiation force for $20 \text{ km} < r < 50 \text{ km}$, where the radiation force is stronger than the other forces in both r - and z -directions. For $50 \text{ km} < r < 200 \text{ km}$, the gas is launched from the accretion disk by the radiation force and moves outward by centrifugal force. The Lorentz force is dominant at $r < r_{\text{M}}$, but as already mentioned, most of the outflows are of disk origin ($r > r_{\text{M}}$). The thermal force, centrifugal force due to the motion in the θ -direction, advection force, and inertial force are significantly small over the whole region. The radial distribution of forces for $r > r_{\text{M}}$ in models B3e9D001, B3e9D01, B1e10D001, B1e10D002, B1e10D004, B3e10D001, B3e10D01, B3e10D02, B3e10D04, and B3e10D1 is similar to that in model B1e10D01. The radial profile of forces outside $r = r_{\text{NS}}$ in models B3e9D01_np and B1e10D1_np, where the magnetosphere is not formed, is the same as that in the disk region outside $r = r_{\text{M}}$ in model B1e10D01.

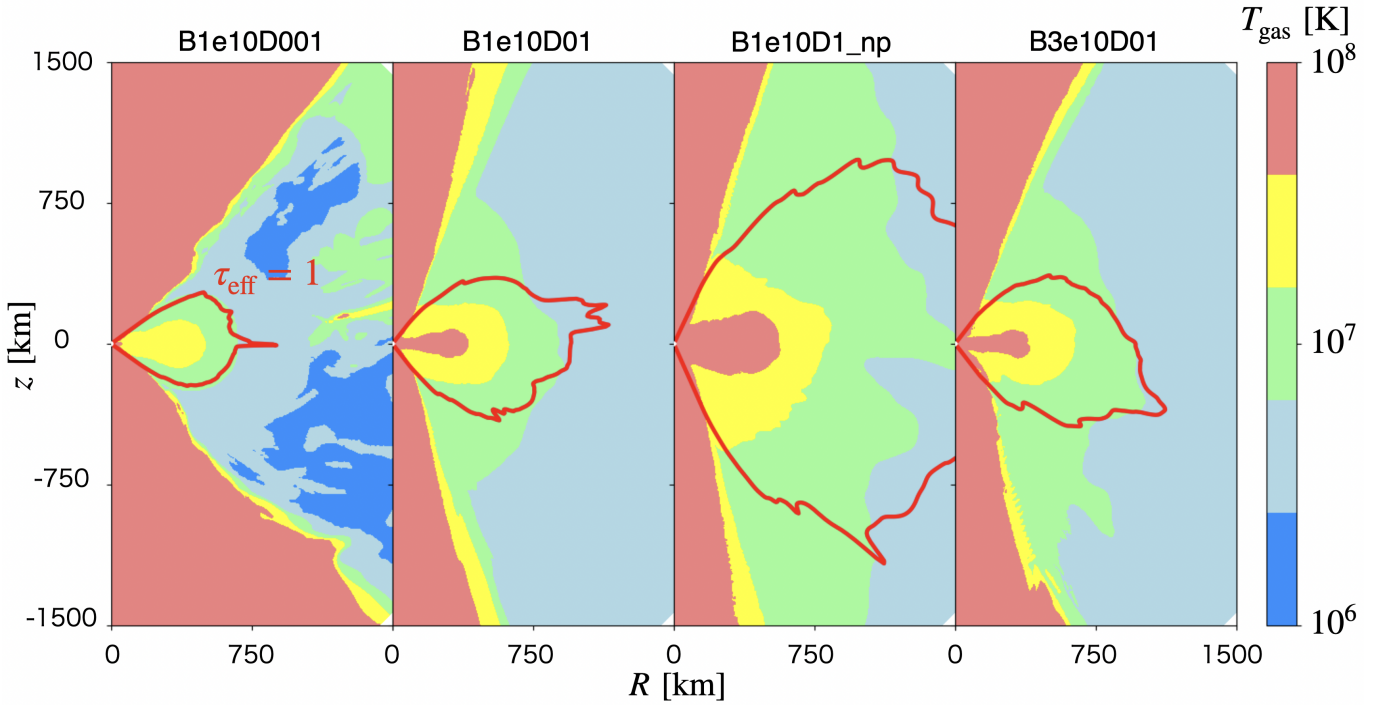


Figure 6. Distributions of time-averaged gas temperature of models B1e10D001, B1e10D01, B1e10D1_np, B3e10D01. Red lines show locations of the photosphere, $\tau_{\text{eff}} = 1$.

In Figure 6, we show the gas temperature distribution and the location of the photosphere. In all models, the gas temperature tends to be high near the z -axis and in the equatorial plane at $r < 750 \text{ km}$. Red lines indicate the

photospheres, $\langle \tau_{\text{eff}} \rangle = 1$, where $\langle \tau_{\text{eff}} \rangle$ is the time-averaged effective optical depth measured as,

$$\langle \tau_{\text{eff}}(r) \rangle = \int_r^{r_{\text{out}}} \langle \rho \rangle \sqrt{\langle \kappa_{\text{abs}} \rangle (\langle \kappa_{\text{abs}} \rangle + \kappa_{\text{sca}})} \sqrt{g_{rr}} dr, \quad (34)$$

where $\langle \kappa_{\text{abs}} \rangle = 6.4 \times 10^{22} \langle \rho \rangle \langle T_{\text{g}} \rangle^{-3.5}$ [$\text{cm}^2 \text{g}^{-1}$]. As can be seen in this figure, the photosphere extends to surround the disk region. The larger the mass accretion rate, the wider the region surrounded by the photosphere. This can be understood from a comparison of models B1e10D001, B1e10D01, and B1e10D1_np. Also, within the range of parameters employed in the present study, the position of the photosphere does not depend much on B_{NS} . It is clear from the fact that the photosphere of models B1e10D01 and B3e10D01 hardly change (see red lines in Figure 6). In all models, the gas temperature on the photosphere is $\sim 10^7$ K over a wide range of polar angles. From this, it is expected that blackbody radiation with a temperature of $\sim 10^7$ K can be observed.

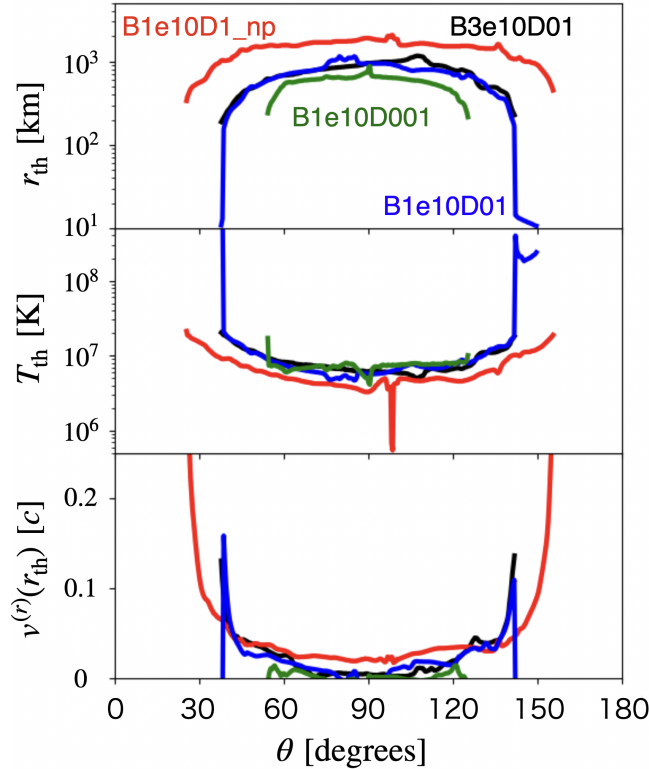


Figure 7. The polar angle (θ) dependencies of the thermalization radius r_{th} (top panel), the gas temperature at the photospheres T_{th} (middle panel), and the gas velocity at the photospheres v_{th} (bottom panel).

Hereafter, we define the thermalization radius r_{th} as the radius where $\langle \tau_{\text{eff}} \rangle = 1$. That is, the radius of the photosphere is represented as r_{th} . In Figure 7, we plot r_{th} (upper panel) and the time-averaged gas temperature at the photospheres T_{th} (middle panel) as a function of polar angle θ . In model B1e10D1_np, which has the largest \dot{M}_{in} in our models, $r_{\text{th}} \gtrsim 1000$ km at $30^\circ < \theta < 150^\circ$. Models with smaller \dot{M}_{in} tend to have smaller r_{th} . The thermalization radius r_{th} is slightly less than 1000 km at $40^\circ < \theta < 140^\circ$ in models B1e10D01 and B3e10D01 and is ~ 500 km at $60^\circ < \theta < 120^\circ$ in model B1e10D001. The thermalization radius cannot be determined close to the rotation axis ($\theta \lesssim 30^\circ$, $150^\circ \lesssim \theta$) since the gas is optically thin and $\langle \tau_{\text{eff}} \rangle < 1$ even at the NS surface. The range of θ , within which r_{th} can be obtained, narrows as \dot{M}_{in} decreases. In all models, T_{th} is almost constant at the angular range where r_{th} can be determined. The bottom panel in Figure 7 shows the polar angle dependence of the radial gas velocity at the photosphere, $v^{(r)}(r_{\text{th}})$, where $v^{(r)} = u^{(r)}/u^{(t)}$. We can see $v^{(r)}(r_{\text{th}}) > 0$ on the photosphere, which indicates that most of the photosphere is located inside the optically thick outflows. Hereafter, we refer to such an outflow as an effectively optically thick outflow (Urquhart & Soria 2016).

Here, we estimate the blackbody temperature T_{bb} by taking θ -averaged T_{th} on the photosphere as

$$T_{\text{bb}} = \frac{1}{\int \sqrt{-g(r_{\text{th}}(\theta), \theta)} d\theta} \int T_{\text{th}}(\theta) \sqrt{-g(r_{\text{th}}(\theta), \theta)} d\theta. \quad (35)$$

This integration is performed on the surface where the thermalization radius can be estimated. The corresponding blackbody radius r_{bb} can be calculated as

$$r_{\text{bb}} = \left[\frac{\langle L_{\text{ISO}} \rangle_{\theta}}{4\pi\sigma T_{\text{bb}}^4} \right]^{1/2}, \quad (36)$$

where the θ -averaged isotropic luminosity $\langle L_{\text{ISO}} \rangle_{\theta}$ is

$$\langle L_{\text{ISO}} \rangle_{\theta} = -\frac{4\pi r_{\text{out}}^2}{\int \sqrt{-g(r_{\text{out}}, \theta)} d\theta} \int \langle R_t^r(r_{\text{out}}) \rangle \sqrt{-g(r_{\text{out}}, \theta)} d\theta. \quad (37)$$

Here, θ integration is also conducted only in the range where the thermalization radius can be obtained. The resulting T_{bb} and r_{bb} are presented in Table 2. The blackbody temperature is not so sensitive to the accretion rate and is $\sim 10^7$ K, which is consistent with the blackbody temperature observed in Swift J0243.6+6124 at the super-Eddington phase (Tao et al. 2019). The resulting r_{bb} is roughly fitted as

$$r_{\text{bb}} = 3.2 \left(\frac{\dot{M}}{\dot{M}_{\text{Edd}}} \right)^{0.71} \text{ [km]}. \quad (38)$$

Tao et al. (2019) showed that the thermal photons would come from $r = 100 - 500$ km for Swift J0243.6+6124. Using equation (38), our model can explain this radius when the accretion rate is $130\dot{M}_{\text{Edd}} < \dot{M}_{\text{in}} < 1200\dot{M}_{\text{Edd}}$. In the models treated in the present study, there is no clear result that r_{bb} depends on B_{NS} . We will discuss this point later.

We run three models, B1e10D001_a, B1e10D001_b, and B1e10D001_c, which have the same initial parameters as model B1e10D001 except for the resolution, to assess the effect of the resolution. We confirm that r_{M} and \dot{M}_{out} of models B1e10D001_a and model B1e10D001_b are almost the same as those of model B1e10D001, while those of model B1e10D001_c are different from those of model B1e10D001. The resolution of the simulation models adopted in this study is the same as or higher than that of model B1e10D001_b. Therefore, our simulation results are independent of the resolution.

3.3. Magnetic field strength of the neutron star in Swift J0243.6+6124

Here, we suggest how to constrain B_{NS} using analytical solutions of r_{M} and \dot{P} and the conditions under which effectively optically thick outflows, which can reproduce the blackbody radiation observed in Swift J0243.6+6124, occur.

It is necessary to simultaneously satisfy $r_{\text{M}} < r_{\text{co}}$, where r_{co} is the corotation radius, and r_{M} can be defined (that is, $r_{\text{M}} > r_{\text{NS}}$) in ULXPs. The condition of $r_{\text{M}} < r_{\text{co}}$ is for gas to accrete onto the NS (Illarionov & Sunyaev 1975). Otherwise, the gas would all be blown away due to the propeller effect. The accretion columns are formed in the case that the second condition is satisfied (see Figure 3 for detail). Substituting equations (24) and (27) into these condition, we get

$$\begin{aligned} B_{\text{NS}} &< 1.6 \times 10^{14} \text{ [G]} \\ &\times \left(\frac{\alpha}{0.1} \right)^{-1/2} \left(\frac{\dot{P}}{-10^{-8} \text{ s s}^{-1}} \right)^{1/2} \\ &\times \left(\frac{M_{\text{NS}}}{1.4M_{\odot}} \right) \left(\frac{r_{\text{NS}}}{10^6 \text{ cm}} \right)^{-2}, \end{aligned} \quad (39)$$

and

$$\begin{aligned} B_{\text{NS}} &> 7.5 \times 10^9 \text{ [G]} \\ &\times \left(\frac{\alpha}{0.1} \right)^{-1/2} \left(\frac{\dot{P}}{-10^{-8} \text{ s s}^{-1}} \right)^{1/2} \left(\frac{M_{\text{NS}}}{1.4M_{\odot}} \right)^{1/2} \\ &\times \left(\frac{r_{\text{NS}}}{10^6 \text{ cm}} \right)^{-1/2} \left(\frac{P}{10 \text{ s}} \right)^{-1}. \end{aligned} \quad (40)$$

If the magnetic field strength at the NS surface satisfies the inequalities of (39) and (40), then the column accretion onto the magnetic poles of the NS appears, and such objects can be the candidates for the ULXPs.

Next, we consider the emergence of the outflows from the super-Eddington disks. The radiatively driven outflows are thought to be launched in the slim disk region, which is inside the spherization radius (or trapping radius), r_{sph} . This is discussed in Shakura & Sunyaev (1973) and revealed by the numerical simulations (Kitaki et al. 2021; Yoshioka et al. 2022). The spherization radius is roughly estimated as $r_{\text{sph}} = (3/2)(\dot{M}_{\text{in}}/\dot{M}_{\text{Edd}})r_{\text{g}}$. Since the disk is truncated at $r = r_{\text{M}}$, the ULXPs accompanying the outflows appear if the condition of $r_{\text{M}} < r_{\text{sph}}$ is satisfied in addition to $r_{\text{NS}} < r_{\text{M}} < r_{\text{co}}$ (Mushtukov et al. 2019). Using equations (24) and (27), $r_{\text{M}} < r_{\text{sph}}$ becomes

$$\begin{aligned} B_{\text{NS}} &< 1.5 \times 10^{12} \text{ [G]} \\ &\times \left(\frac{\alpha}{0.1}\right)^{-1/2} \left(\frac{\dot{P}}{-10^{-8} \text{ s s}^{-1}}\right)^{3/2} \\ &\times \left(\frac{M_{\text{NS}}}{1.4M_{\odot}}\right) \left(\frac{P}{10 \text{ s}}\right)^{-3}. \end{aligned} \quad (41)$$

Equations (39)-(41) are the general conditions to explain the ULXPs, while we concentrate on the discussion about Swift J0243.6+6124 in the following. As described in Section 3.2, the range of the mass accretion rate that can reproduce the blackbody radiation observed in this object is $130\dot{M}_{\text{Edd}} < \dot{M}_{\text{in}} < 1200\dot{M}_{\text{Edd}}$ from relation (38). Using equation (27), this condition is transformed as

$$\begin{aligned} B_{\text{NS}} &< 9.8 \times 10^{11} \text{ [G]} \\ &\times \left(\frac{\alpha}{0.1}\right)^{-1/2} \left(\frac{\dot{P}}{-10^{-8} \text{ s s}^{-1}}\right)^{7/2} \left(\frac{M_{\text{NS}}}{1.4M_{\odot}}\right)^{-1} \\ &\times \left(\frac{r_{\text{NS}}}{10^6 \text{ cm}}\right)^4 \left(\frac{P}{10 \text{ s}}\right)^{-7}, \end{aligned} \quad (42)$$

$$\begin{aligned} B_{\text{NS}} &> 1.3 \times 10^9 \text{ [G]} \\ &\times \left(\frac{\alpha}{0.1}\right)^{-1/2} \left(\frac{\dot{P}}{-10^{-8} \text{ s s}^{-1}}\right)^{7/2} \left(\frac{M_{\text{NS}}}{1.4M_{\odot}}\right)^{-1} \\ &\times \left(\frac{r_{\text{NS}}}{10^6 \text{ cm}}\right)^4 \left(\frac{P}{10 \text{ s}}\right)^{-7}. \end{aligned} \quad (43)$$

Among ULXPs with outflows, objects that meet the conditions (41) and (42) would have effectively optically thick outflows, and the blackbody radiation with $r_{\text{bb}} > 100$ km would appear in the radiation spectrum.

Figure 8 summarizes the conditions shown above in the $\dot{P} - B_{\text{NS}}$ plane. Here, we assume $P = 9.8$ s, which is the rotation period observed in Swift J0243.6+6124 (Doroshenko et al. 2018; Chen et al. 2021). We take $\alpha = 0.1$, $M_{\text{NS}} = 1.4M_{\odot}$, and $r_{\text{NS}} = 10$ km. The red shaded region indicates the ULXP with outflow, which satisfies both $r_{\text{NS}} < r_{\text{M}} < r_{\text{co}}$ and $r_{\text{M}} < r_{\text{sph}}$. The ULXP without outflow is in the white region, where $r_{\text{NS}} < r_{\text{M}} < r_{\text{co}}$ is satisfied but $r_{\text{M}} < r_{\text{sph}}$ is not satisfied. The condition of ULXPs such as $r_{\text{M}} > r_{\text{co}}$ (propeller regime) or $r_{\text{M}} < r_{\text{NS}}$ (non-pulsating regime) is not satisfied in grey shaded regions. In the blue hatched region where the accretion rate is $130\dot{M}_{\text{Edd}} < \dot{M}_{\text{in}} < 1200\dot{M}_{\text{Edd}}$, effectively optically thick outflows with $r_{\text{bb}} = 100 - 500$ km and $T_{\text{bb}} \sim 10^7$ K appear so that the blackbody radiation, as observed in Swift J0243.6+6124, is thought to be reproduced. Here, it is confirmed that the models that can successfully reproduce such effectively optically thick outflows and accretion columns (B1e10D004, B1e10D01, B3e10D01, and B3e10D02) are located in the blue hatched region (filled circles). In contrast, other models are located outside the blue hatched region (filled squares). In observations of Swift J0243.6+6124, P is almost constant, while \dot{P} is reported to be $-2.22 \times 10^{-8} \text{ s s}^{-1}$ (Obs. 1), $-1.75 \times 10^{-8} \text{ s s}^{-1}$ (Obs. 2), and $-6.8 \times 10^{-9} \text{ s s}^{-1}$ (Obs. 3) (Doroshenko et al. 2018; Chen et al. 2021). These observed spin-up rates are denoted by black dashed lines in Figure 8. In Obs. 1 and 2, the observed isotropic luminosity exceeds L_{Edd} , and the thermal emission of which the observed blackbody radius is 100 – 500 km is observed (obsID: 90302319004, 90302319006 and 90302319008 in Tao et al. 2019). Then, the magnetic field strength is restricted to be $2 \times 10^{10} \text{ G} < B_{\text{NS}} < 5 \times 10^{12} \text{ G}$ for Obs. 1 and $10^{10} \text{ G} < B_{\text{NS}} < 4 \times 10^{12} \text{ G}$ for Obs. 2, which are represented by black solid lines. In Obs. 3, on the other hand, the

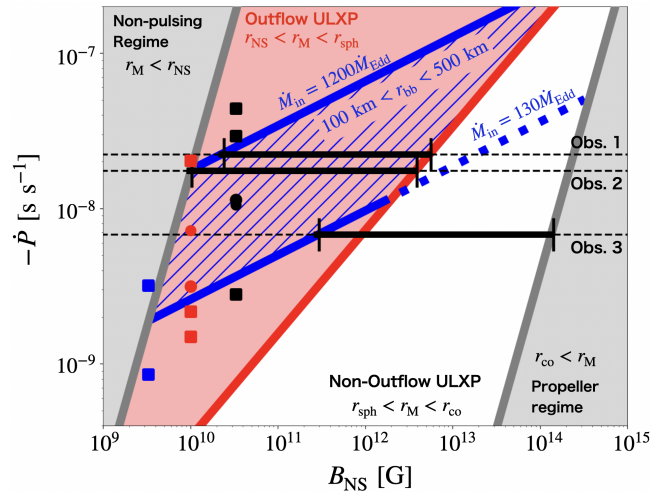


Figure 8. Here, the conditions (39)-(43) are summarized in the $\dot{P} - B_{\text{NS}}$ plane (see text for detail). The spin-up rates of models B1e10D004, B1e10D01, B3e10D01, and B3e10D02 are shown by filled circles, while square markers are that of the other models. We employ table 1 in Chen et al. (2021) for the observed \dot{P} (see also Doroshenko et al. 2018). Parameters for the conditions: $\alpha = 0.1$, $M_{\text{NS}} = 1.4M_{\odot}$, $r_{\text{NS}} = 10^6$ cm, and $P = 9.8$ s.

luminosity is lower than L_{Edd} , and the thermal emission is not observed. Such features are realized in the condition that the magnetic field is in the range of $3 \times 10^{11} \text{ G} < B_{\text{NS}} < 10^{14} \text{ G}$ (see black solid line for Obs. 3). Therefore, the magnetic field strength that satisfies the three observations is between $3 \times 10^{11} \text{ G}$ and $4 \times 10^{12} \text{ G}$. Using the equation (27), the mass accretion rate corresponding to this range is estimated to be $200\dot{M}_{\text{Edd}} \lesssim \dot{M}_{\text{in}} \lesssim 500\dot{M}_{\text{Edd}}$ for Obs. 1 and 2, and $60\dot{M}_{\text{Edd}} \lesssim \dot{M}_{\text{in}} \lesssim 100\dot{M}_{\text{Edd}}$ for Obs. 3. Since the luminosity has been reported to be $\sim 10^{39} \text{ erg s}^{-1}$ at the super-Eddington phase in Swift J0243.6+6124 (Obs.1 and 2), the radiative efficiency of this object is 1-5%, which is smaller than the standard accretion efficiency. This indicates that Swift J0243.6+6124 is observed at a relatively large viewing angle within the range where the pulse emission is detected. The magnetic field strength evaluated in the present study is not inconsistent with previous studies (Tsygankov et al. 2018; Doroshenko et al. 2020). Tsygankov et al. (2018) estimated the upper limit for B_{NS} in Swift J0243.6+6124, $< 6 \times 10^{12} \text{ G}$, from the fact that the transition to the propeller regime was not detected even at a luminosity of $6 \times 10^{35} \text{ erg s}^{-1}$. Doroshenko et al. (2020) concluded that B_{NS} in Swift J0243.6+6124 is in $(3-9) \times 10^{12} \text{ G}$ and likely at the lower limit of this range. We note that B_{NS} here is assumed not to change during the observation. This assumption would be reasonable since it has been pointed out that the NS magnetic field strength does not change for a sufficiently long period, $> 1 \text{ Myr}$, based on the observations of some X-ray pulsars and the ULXP, NGC 1313 X-2 (Makishima et al. 1999; Sathyaprakash et al. 2019). Although the NSs might have multipole magnetic fields, we focus on the case of the dipole magnetic fields in this study. We will discuss multipole fields later.

4. DISCUSSIONS

4.1. Geometrical beaming

In our all models, the radiation is highly beamed by the outflows from the accretion disk. The amplification factor $\langle L_{\text{iso}} \rangle / \langle L_{\text{rad}} \rangle \equiv 1/b$ exceeds 100 at maximum, which is higher than that indicated by King & Lasota (2019) (typically $1/b \sim 1-10$) (see also Takahashi & Ohsuga 2017; Abarca et al. 2021). The cause of this difference is probably the magnetic field strength. The difference will be smaller if we employ a strong B_{NS} by which r_{M} nearly equals r_{sph} , although r_{M} is much smaller than r_{sph} in the present study. As r_{M} approaches r_{sph} , the outflow rate would decrease since the outflows mainly occur in $r_{\text{M}} < r < r_{\text{sph}}$. In this case, the outflow can no longer effectively collimate the radiation, and therefore $1/b$ would decrease (Abarca et al. 2021). Although simulating $r_{\text{M}} \sim r_{\text{sph}}$ is difficult and beyond the scope of the present study (see also Section 4.5), we plan to conduct such simulations in the future.

4.2. Comparison with observations of NGC 5907 ULX1 and NGC 1313 X-2

Here, we show, based on the present simulations, that the ULXPs, NGC 5907 ULX1 and NGC 1313 X-2, are thought to be powered by the highly super-Eddington accretion onto NSs with relatively weak magnetic fields. In NGC 5907

ULX1, the mechanical power ($L_{\text{mec}}^{\text{obs}}$), which is evaluated from the observed nebula emission of the ULX bubbles, is reported to 1.3×10^{41} erg s $^{-1}$ (Belfiore et al. 2020), and is comparable to $\langle L_{\text{kin}} \rangle$ for the higher mass accretion rate model (B3e10D1), $\sim 8 \times 10^{40}$ erg s $^{-1}$. In addition, the isotropic luminosity $\langle L_{\text{ISO}} \rangle$ in model B3e10D1 at $\theta \sim 30^\circ$ or 150° is almost the same as the observed X-ray luminosity, $L_{\text{ISO}}^{\text{obs}} \sim 2.2 \times 10^{41}$ erg s $^{-1}$ (Israel et al. 2017a), where the isotropic luminosity is calculated as $\langle L_{\text{ISO}} \rangle = -4\pi r_{\text{out}}^2 \langle R_t^r \rangle$. Thus, NGC 5907 ULX1 probably has a mass accretion rate of $> 10^3 \dot{M}_{\text{Edd}}$ and is viewed from at the polar angle 20-30 degrees away from the z -axis. The magnetic field strength of the NS is stronger than 10^{10} G. This is because $\langle L_{\text{kin}} \rangle$ and $\langle L_{\text{ISO}} \rangle$ of model B1e10D1_np are almost the same as those of model B3e10D1, but no accretion column appears in this model.

Also, $\langle L_{\text{kin}} \rangle$ for our slightly lower mass accretion models (B1e10D01, B3e10D01, and B3e10D02) are comparable to $L_{\text{mec}}^{\text{obs}}$ in NGC 1313 X-2, $\sim 10^{40}$ erg s $^{-1}$ (Pakull & Grisé 2008). In these models, the viewing angle, at which L_{ISO} is consistent with $L_{\text{ISO}}^{\text{obs}} \sim (1.4 - 2.0) \times 10^{40}$ erg s $^{-1}$, is about 30 to 40 degrees measured from the z -axis. Therefore, NGC 1313 X-2 would be almost a face-on object with a mass accretion rate of several $10^2 \dot{M}_{\text{Edd}}$. Since no accretion column is formed in model B3e9D01_np, of which the kinetic and isotropic luminosity are similar to those of the above three models, B_{NS} would be stronger than 3.3×10^9 G.

According to our numerical models, both NGC 5907 ULX1 and NGC 1313 X-2 would also have effectively optically thick outflows with $r_{\text{bb}} > 100$ km. Indeed, the thermal emission, probably originated from outflows, was reported in NGC 1313 X-2 (Qiu & Feng 2021). However, such emission is not detected in NGC 5907 ULX1. This inconsistency can be resolved by conducting simulations of a large r_{M} . If B_{NS} is so strong that r_{M} is comparable to r_{sph} , then the outflow rate is thought to decrease, and thermal emission is not detected. In this case, $1/b$ decreases as discussed in Section 4.1, and the observer's viewing angle should be smaller than that estimated above for $\langle L_{\text{ISO}} \rangle$ to be consistent with $L_{\text{ISO}}^{\text{obs}} \sim (1.4 - 2.0) \times 10^{41}$ erg s $^{-1}$. However, increasing B_{NS} may change the intrinsic luminosity, and therefore simulations with a high B_{NS} is necessary to perform. Post-processing radiative transfer simulations are needed to obtain detailed radiation spectra and compare the observation (Kawashima et al. 2012; Kitaki et al. 2017; Narayan et al. 2017).

On the other hand, no nebular has been detected around Swift J0243.6+6124. The reason is that the object is a transient source. In order to form a nebula extending over 100 pc, an energy injection, $\sim 10^{40}$ erg s $^{-1}$, from the central object is needed to last for at least 10^5 yr (Pakull & Grisé 2008; Belfiore et al. 2020).

4.3. Ultraluminous supersoft sources

Our simulations are consistent with the hypothesis proposed by Urquhart & Soria (2016) in which ULXs are observed as ultraluminous supersoft sources (ULSs) by an edge-on observer, as far as the angular range of $\tau_{\text{eff}} > 1$ and its accretion rate dependence are concerned. According to their model, the optical depth of the outflows τ_{eff} is larger than unity at $35^\circ < \theta < 145^\circ$ for $\dot{M}_{\text{in}} \sim 100 \dot{M}_{\text{Edd}}$, and the polar angle at which $\tau_{\text{eff}} > 1$ widens as the mass accretion rate increases. These features are also obtained in our simulations. Indeed, simulated outflows are effectively optically thick at polar angles greater than 40 degrees away from the z -axis for models B1e10D01 and B3e10D01 (see Figures 6 and 7 for detail). The mass accretion rates in these models are $500 \dot{M}_{\text{Edd}}$ and $720 \dot{M}_{\text{Edd}}$, respectively (Table 2). This angular range and the mass accretion rates do not so contradict the suggestion by Urquhart & Soria (2016) mentioned above. Other models, in which the accretion rate is $\sim 10^{2-3} \dot{M}_{\text{Edd}}$ and the accretion columns form, show approximately the same results. In addition, the angular range where $\tau_{\text{eff}} > 1$ widens with increasing in the mass accretion rate (see Figure 7). However, the blackbody temperature estimated from the simulation, $\sim 10^7$ K, is higher than that observed in the ULSs, $\sim 10^6$ K. Such a discrepancy might be resolved by the simulations with the initial torus located far away since the winds launched from the outer part of the accretion disks work to expand the photosphere and lower the temperature there (we will discuss this point later). If this is the case, our simulations are consistent with the hypothesis in which ULSs are edge-on sources of ULXs.

4.4. Why does the one-side accretion occur?

The accretion to only one of the poles (one-side accretion) occurs in models with a relatively large truncation radius (B3e9D001, B1e10D001, B1e10D002, B3e10D001, B3e10D01, and B3e10D02) since the distorted magnetic field lines inhibit the gas accretion onto the opposite side. Initially, the shape of the NS magnetic field is symmetric with respect to the equatorial plane. Then, the magnetic field on the equatorial plane is perpendicular to the equatorial plane. However, when the gas accumulates at the truncation radius and flows toward either pole, the magnetic field lines are distorted (see magnetic field lines in the left panel of Figure 3). The magnetic field on the equatorial plane at the

truncation radius will be tilted with respect to the equatorial plane. Since the gas tends to move to the side with the lower gravitational potential, the gas flows in the direction in which the preceding gas accretes. The accretion column on the opposite side is less likely to be formed. This one-side accretion is more pronounced for the model with a large truncation radius (B3e9D001, B1e10D001, B1e10D002, B3e10D001, B3e10D01, and B3e10D02). In contrast, for the case where the truncation radius is very small, the gas on the surface of the thick disk accretes to the opposite pole, forming two accretion columns (models B1e10D01, B1e10D004, B3e10D04, and B3e10D1). The one-side accretion described above was also shown by some MHD simulations (see e.g., Lii et al. 2014; Takasao et al. 2022). We discuss the importance of three-dimensional simulations to study the detailed structure of accretion flow in the subsequent section.

4.5. Future issues

Three-dimensional simulations of non-axisymmetric accretion flows onto a rotating NS have yet to be performed. In this study, we assume an axisymmetric structure, in which the magnetic axis of the NS coincides with the rotation axis of the accretion disk, and perform two-dimensional simulations. However, the gas is thought to accrete onto the NS surface through multiple streams due to the magnetic Rayleigh–Taylor or interchange instability (Kulkarni & Romanova 2008). Furthermore, the pulse emission is produced by the misalignment between the magnetic axis and rotation axis of the NS. Thus, we need to treat a non-axisymmetric structure with three-dimensional simulations. The misalignment of two axes might make the one-side accretion difficult to occur since the gas in the accretion disk would preferentially accrete to the closest pole (see e.g., Romanova et al. 2003). In addition, if the NS rotates as fast as millisecond pulsars, the outflow rate might increase due to the effective acceleration by a rapidly rotating magnetosphere of the NS (e.g., Lovelace et al. 1999). Since the size of the photosphere increases as the mass outflow rate increases, the gas temperature decreases. As a result, r_{bb} increases, and B_{NS} is larger than that estimated in Figure 8. Simulations taking account of the rotation of the NS have been performed by Parfrey & Tchekhovskoy (2017) and Das et al. (2022).

In our simulations, the gas-radiation interaction is switched off in the very vicinity of the rotation axis near the NS where $\sigma > \sigma_{\text{rad}}$ (see Section 2.3). This treatment would not affect the resulting size and temperature of the photosphere in Section 3.2. In the present simulations, the radiatively driven outflows are launched from the accretion column base as well as the accretion disk (see also Abolmasov & Lipunova 2022). However, the opacity of free-free absorption of such outflows is quite small due to the low-density and high temperature. This leads to the smaller size of the photosphere for $\theta \lesssim \pi/6, 5\pi/6 \lesssim \theta$ compared with that formed by outflows from the accretion disk ($r_{\text{th}} \sim$ several 100 km, see red lines in Figure 6). If we do not ignore the gas-radiation interaction near the rotation axis, the outflowing gas launched from the accretion column is more effectively accelerated by the radiation force near the rotation axis. This further reduces the gas density and size of the photosphere. Therefore, neglecting the gas-radiation interaction in the vicinity of the rotation axis near the NS does not affect the size and temperature of the photosphere presented in Section 3.2.

We need to investigate the influence of the boundary condition. In this study, we assumed that the kinetic and thermal energy reaching the inner boundary (NS surface) is immediately converted into radiative energy. Under this boundary condition, the energy carried to the NS core is ignored. In reality, a fraction of the energy reaching the NS surface is converted into the thermal energy of the NS atmosphere. The heat flux from the atmosphere to the core occurs due to thermal conduction (see Wijnands et al. 2017, and references therein). Then, the radiative energy generated on the NS surface might decrease, leading to a decrease in radiative luminosity. Also, the accretion flow geometry might change if we set different boundary conditions (see Appendix A for detail). Investigation of how the accretion flow depends on the boundary conditions is left as future work.

GR-RMHD simulations of large-scale accretion flows are also needed to evaluate r_{bb} and T_{bb} , more accurately. It has been pointed out that the simulations in which the initial torus is located inside the spherization radius overestimate the mass outflow rate (see Kitaki et al. 2021; Yoshioka et al. 2022). Therefore, the accretion rate to reproduce effectively optically thick outflows would be higher than that estimated in the present study. This point should be clarified in long-term simulations with the initial torus placed far enough away from the spherization radius. In such simulations, the disk wind is expected to blow from the outer region of the accretion disks ($r \lesssim r_{\text{sph}}$). The blackbody radius would be larger, and the blackbody temperature would be smaller in the region near the equatorial plane. If this is the case, edge-on observers might identify the objects as the ULs.

In the present study, we adopt a relatively weak magnetic field of the NS $3.3 \times 10^{9-10}$ G compared to the typical X-ray pulsar 10^{11-13} G. As B_{NS} increases while the accretion rate remains fixed, the amount of the outflowing gas probably reduces since the area where radiatively driven outflows mainly occur, $\pi(r_{\text{sph}}^2 - r_{\text{M}}^2)$, decreases. This leads the photosphere to be small and the gas temperature at the photosphere to be high. It is expected that the blackbody radius tends to decrease with an increase in B_{NS} . In this case, the magnetic field strength of Swift J0243.6+6124 estimated in Section 3.3 would decrease. Although r_{bb} may depend on B_{NS} as described above, r_{bb} is a function of mass accretion rate only (see Table 1 and equation 38) in our results since simulations of $r_{\text{M}} \ll r_{\text{sph}}$ are performed. In addition, it has been reported that when B_{NS} is strong enough that $r_{\text{M}} > r_{\text{sph}}$, r_{M} is no longer dependent on B_{NS} (Chashkina et al. 2017). We need to perform simulations for the strong B_{NS} case.

The M1 closure, which is employed in the present study, leads to unphysical solutions when the system is optically thin and the radiation fields are anisotropic (see e.g., Ohsuga & Takahashi 2016). In our simulations, especially in the models where the one-side accretion occurs, the radiation fields are quite anisotropic. In order to accurately calculate the radiation fields, we have to solve the radiative transfer equation. Such radiation MHD simulations, in which the radiative transfer equation is solved, are performed by Jiang et al. (2014), Ohsuga & Takahashi (2016), Asahina et al. (2020), Zhang et al. (2022), and Asahina & Ohsuga (2022).

The modeling of Swift J0243.6+6124 considering multipolar magnetic field components is to be further investigated. Although we constrain the dipole magnetic field strength at the NS surface, $3 \times 10^{11} \text{ G} < B_{\text{NS}} < 4 \times 10^{12} \text{ G}$, in the present work (see also Tsygankov et al. 2018; Doroshenko et al. 2020), a cyclotron resonance scattering feature (CRSF) corresponding to $1.6 \times 10^{13} \text{ G}$ was reported by Kong et al. (2022). This discrepancy is resolved if CRSF originates from multipole magnetic fields, as already suggested by some authors (see e.g., Israel et al. 2017a). In the case that the multipole magnetic field component is dominant over the dipole component, the accretion flow geometry is expected to be more complex (Long et al. 2007; Das et al. 2022), and the position of the magnetospheric radius changes. We plan to perform the GR-RMHD simulations of super-Eddington accretion flows onto the NS with multipole magnetic fields.

Our models might exhibit a high polarization degree, as recently observed in the X-ray binary (Veledina et al. 2023; Ratheesh et al. 2023). The hard X-ray photons produced in the accretion column base are scattered by the inner wall of funnel, which consists of the effectively optically thick outflows, and pass through the low-density region near the rotation axis. If such photons are observed, a high polarization degree might be detected. Indeed, Ratheesh et al. (2023) reported that the polarization degree increases from approximately 6% at 2 keV to 10% at 8 keV. Post-process polarized radiative transfer simulations are needed to compare our models with such observations.

5. CONCLUSIONS

We performed two-dimensional axisymmetric GR-RMHD simulations of super-Eddington flows around NSs with a dipole magnetic field for modeling the galactic ULXP, Swift J0243.6+6124. In our simulations, the accretion columns near the magnetic poles, the super-Eddington disk outside the magnetospheric radius, and outflows launched from the disk appear. If the magnetospheric radius (truncation radius) is smaller than the spherization radius, the outflows are generated since the radiation force mainly drives the outflows inside the spherization radius. When the accretion rate is large enough while satisfying the above condition, effectively optically thick outflows are launched from the disk and would be responsible for the blackbody radiation. The blackbody temperature of the effectively thick outflow, $\sim 10^7 \text{ K}$, is roughly consistent with the observations by Tao et al. (2019). The blackbody radius increases with an increase in the mass accretion rate and agrees with observations, 100 – 500 km, when the accretion rate is about $(130 - 1200)\dot{M}_{\text{Edd}}$. Since the blackbody radiation was detected in two observations with \dot{P} of $-2.22 \times 10^{-8} \text{ s s}^{-1}$ and $-1.75 \times 10^{-8} \text{ s s}^{-1}$, but not in another with $\dot{P} \sim -6.8 \times 10^{-9} \text{ s s}^{-1}$, the surface magnetic field strength of the NS in Swift J0243.6+6124 is limited to be $3 \times 10^{11} \text{ G} \lesssim B_{\text{NS}} \lesssim 4 \times 10^{12} \text{ G}$. The accretion rate is evaluated to be $(200 - 500)\dot{M}_{\text{Edd}}$ when the blackbody radiation is detected and $(60 - 100)\dot{M}_{\text{Edd}}$ when the blackbody radiation is not observed. Our results support the hypothesis that the super-Eddington phase in the 2017-2018 giant outburst of Swift J0243.6+6124 is powered by super-Eddington accretion flows onto a magnetized NS.

We would like to thank an anonymous reviewer for fruitful comments. This work was supported by JSPS KAKENHI Grant Numbers JP21J21040 (A.I.), JP21H04488, JP18K03710 (K.O.), JP20K11851, JP20H01941, JP20H00156 (H.R.T) and JP18K13591 (Y.A.). A part of this research has been funded by the MEXT as "Program for Promoting Researches on the Supercomputer Fugaku" (Toward an unified view of the universe: from large scale structures to planets, JPMXP1020200109) (K.O., H.R.T., Y.A., and A.I.), and by Joint Institute for Computational Fundamental Science (JICFuS, K.O.). Numerical computations were performed with computational resources provided by the Multidisciplinary Cooperative Research Program in the Center for Computational Sciences, University of Tsukuba, Oakforest-PACS operated by the Joint Center for Advanced High-Performance Computing (JCAHPC), Cray XC 50 at the Center for Computational Astrophysics (CfCA) of the National Astronomical Observatory of Japan (NAOJ), the FUJITSU Supercomputer PRIMEHPC FX1000 and FUJITSU Server PRIMERGY GX2570 (Wisteria/BDEC-01) at the Information Technology Center, The University of Tokyo.

APPENDIX

A. DEPENDENCE OF THE ACCRETION FLOWS ON THE BOUNDARY CONDITIONS

Here, we show the dependence of the accretion flows on the inner boundary condition of the radiative flux. Figure 9 shows the time evolution of the gas density and radiation energy density with different boundary conditions. The top panel is the result of model **Be10D01** where the radiative flux at the NS surface is set to zero. On the other hand, the results of the model in which the radiative flux is set according to the free boundary condition are presented in the bottom panel (free boundary model). Cyan lines show the magnetic field lines. We can see that the low-density void region is formed between two accretion columns ($10 \text{ km} < r < 13 \text{ km}$ and $50^\circ < \theta < 130^\circ$). A part of the photons emitted from the accretion columns is transported to the void region. These photons push the gas outward and the void is suffered from expansion (see, the right top panel of Figure 9). This void repeatedly contracts and expands. The period of repeated expansion is about $\sim 500t_g \simeq 10^{-3} \text{ s}$. However, the variation in the mass accretion rate at the NS surface due to the expansion is negligibly small. Such a structure can not be seen in the free boundary model. This is because the photon can freely penetrate the NS surface, and the outward radiation force considerably becomes small compared with model **B1e10D01**.

We also find that the thickness of the accretion column in the free boundary model is thinner than that of model **B1e10D01**. It may originate from the decrease in the radiation energy of the accretion column due to the free boundary condition. It can be seen that the radiation energy at the base of the accretion column in model **B1e10D01** is about one hundred times larger than that in the free boundary model.

B. ANALYTIC FORMULA OF MAGNETOSPHERIC RADIUS AND SPIN-UP RATE

Takahashi & Ohsuga (2017) derived the analytical formulas of the magnetospheric radius (24), and spin-up rate (27), applying the self-similar solutions for the slim disk proposed by Watarai & Fukue (1999). Here we summarize the derivations of these formulas.

In the slim disk model, the energy balances are $Q_{\text{adv}}^- = Q_{\text{vis}}^+ + Q_{\text{rad}}^- = fQ_{\text{vis}}^+$ (Narayan & Yi 1994), where Q_{adv}^- is the advected energy, Q_{vis}^+ is the viscous-dissipated energy, Q_{rad}^- is the radiative cooling energy, and f represents the fraction of the advective cooling to the viscous-dissipated energy. Using the height-integrated radiation pressure described in equation 12 in Watarai & Fukue (1999) and the scale height of the accretion disk H , presented in equation 11 in Watarai & Fukue (1999), we get

$$p_{\text{rad}} = \Pi_{\text{rad}}/2H = \frac{\dot{M}}{4\pi\alpha} \frac{c_3^{1/2}}{c_1} \sqrt{\frac{GM_{\text{NS}}}{r^5}}, \quad (\text{B1})$$

where α is the viscous parameter (Shakura & Sunyaev 1973), c_1 and c_3 is the constant depending on Γ , f and α (see Watarai & Fukue 1999, for detail). In this study, we take $\Gamma = 1.5$, $f = 0.1$ for the analytical formula. The reason why we do not employ $\Gamma = 5/3$ is that the rotational velocity of the disk is zero with $\Gamma = 5/3$ (Narayan & Yi 1994). The magnetic pressure at radius r by the dipole magnetic field is $p_{\text{mag}} = B_{\text{NS}}^2/8\pi(r_{\text{NS}}/r)^6$. The magnetospheric radius r_{M}

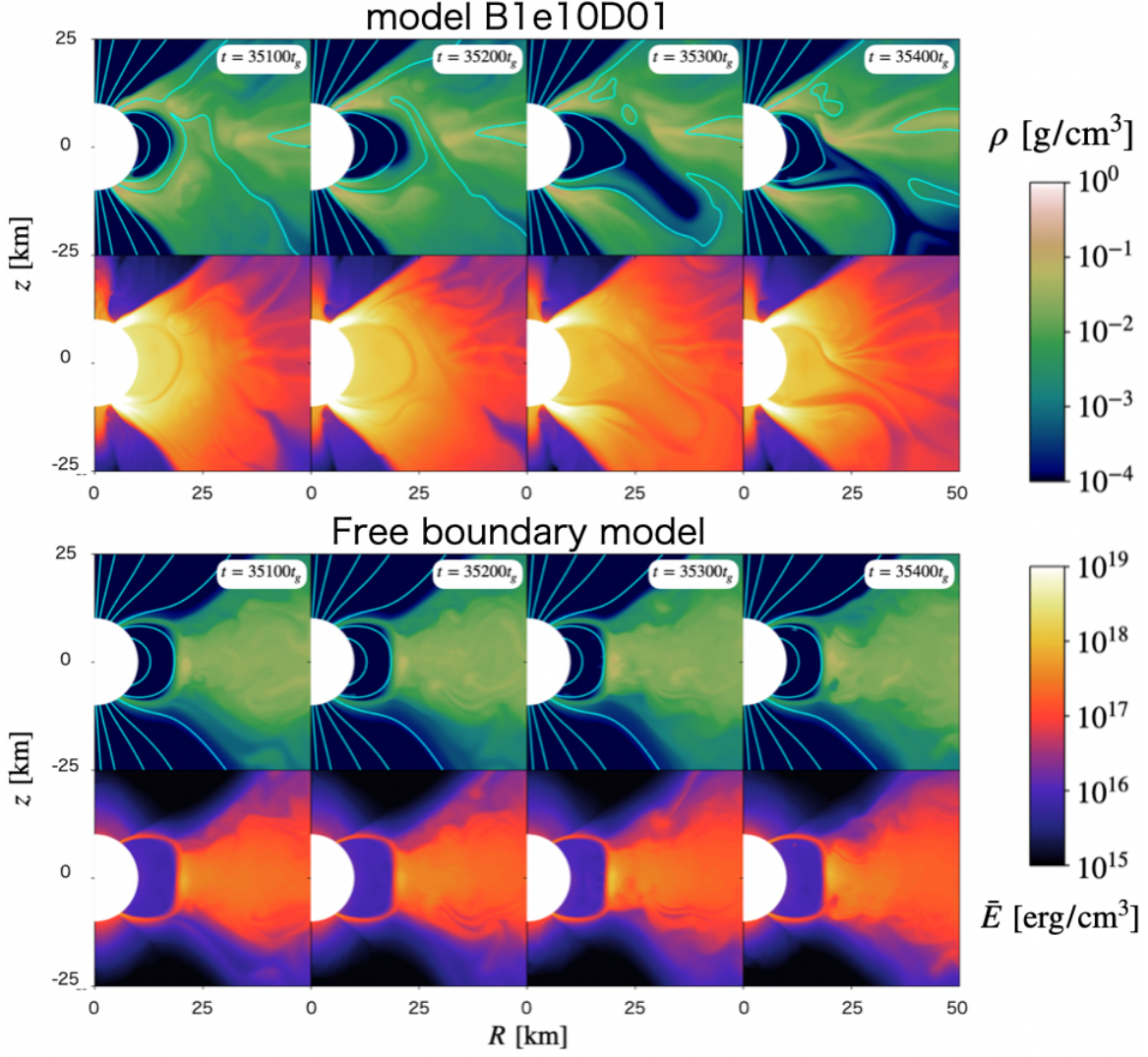


Figure 9. Time evolution of the mass density and the radiation energy density. The colors show the gas density and radiation energy density. The cyan lines represent the magnetic field lines. The top panel is the results of model B1e10D01. The results of the model, where the free boundary condition is adopted for radiative flux (free boundary model), are presented in the bottom panel. All the same initial parameters as B1e10D01 are adopted in the free boundary model except for the boundary condition of the radiative flux.

is defined as the radius where p_{mag} balances with p_{rad} :

$$r_M = \left(\frac{1}{8\pi} \frac{c_1}{c_3^{1/2}} \frac{c\kappa_{\text{sca}}}{G^{3/2}} \right)^{2/7} \times \alpha^{2/7} \left(\frac{\dot{M}_{\text{in}}}{\dot{M}_{\text{Edd}}} \right)^{-2/7} B_{\text{NS}}^{4/7} M_{\text{NS}}^{-3/7} r_{\text{NS}}^{12/7}. \quad (\text{B2})$$

Next we give the derivation of the spin-up rate. The spin-up rate can be calculated by assuming that the Keplerian angular momentum at r_M is transported to the NS without dissipation. In this case, spin-up rate is represented by $\dot{P} = -\dot{M}l(r_M)/M_{\text{NS}}l_{\text{NS}}$ (Shapiro & Teukolsky 1986), where $l = \sqrt{GM_{\text{NS}}r}$ is the specific Keplerian angular momentum. Using (B2), the spin-up can be calculated as follows:

$$\dot{P} = -\frac{2G^{3/2}}{c\kappa_{\text{sca}}} \left(\frac{1}{8\pi} \frac{c_1}{c_3^{1/2}} \frac{c\kappa_{\text{sca}}}{G^{3/2}} \right)^{1/7}$$

$$\begin{aligned}
& \times \alpha^{1/7} \left(\frac{\dot{M}_{\text{in}}}{\dot{M}_{\text{Edd}}} \right)^{6/7} \\
& \times B_{\text{NS}}^{2/7} M_{\text{NS}}^{2/7} r_{\text{NS}}^{-8/7} P^2.
\end{aligned} \tag{B3}$$

C. EQUATIONS OF MOTION IN GENERAL RELATIVITY

Here, we derive the equations of motion, which are used in this study, according to [Mihalas & Mihalas \(1984\)](#). Equation (2) can be transformed to

$$\partial_\mu T^{\mu\nu} = -T^{\mu\nu} \frac{\partial_\mu \sqrt{-g}}{\sqrt{-g}} - \Gamma_{\alpha\mu}^\nu T^{\alpha\mu} + G^\nu. \tag{C4}$$

Subtracting the time component of (C4) multiplied by u^i/u^t from the spatial component of (C4), the following relation can be obtained:

$$\begin{aligned}
& \partial_\mu T^{\mu i} - \frac{u^i}{u^t} \partial_\mu T^{\mu t} \\
& = - \left(T^{\mu i} - \frac{u^i}{u^t} T^{\mu t} \right) \frac{\partial_\mu \sqrt{-g}}{\sqrt{-g}} \\
& \quad - \left(\Gamma_{\alpha\mu}^i - \frac{u^i}{u^t} \Gamma_{\alpha\mu}^t \right) T^{\alpha\mu} + G^i - \frac{u^i}{u^t} G^t.
\end{aligned} \tag{C5}$$

We define the relativistic enthalpy, $w = \rho + p_{\text{gas}} + e + b^2$, and equation (C5) can be written as

$$\begin{aligned}
\partial_\mu T^{\mu i} - \frac{u^i}{u^t} \partial_\mu T^{\mu t} & = w u^\mu \left[\partial_\mu \left\{ e_{(\alpha)}^i \right\} - \frac{u^i}{u^t} \partial_\mu \left\{ e_{(\alpha)}^t \right\} \right] u^{(\alpha)} \\
& \quad + w \left[e_{(\alpha)}^i - \frac{u^i}{u^t} e_{(\alpha)}^t \right] \frac{du^{(\alpha)}}{d\tau} \\
& \quad + \partial_\mu \left\{ (p_{\text{gas}} + p_{\text{mag}}) g^{\mu i} \right\} \\
& \quad - \frac{u^i}{u^t} \partial_\mu \left\{ (p_{\text{gas}} + p_{\text{mag}}) g^{\mu t} \right\} \\
& \quad - \partial_\mu (b^\mu b^i) + \frac{u^i}{u^t} \partial_\mu (b^\mu b^t),
\end{aligned} \tag{C6}$$

where $e^{(\mu)}_\alpha$ is the orthonormal tetrad that transforms vectors in the laboratory frame (e.g., Boyer–Lindquist coordinate) to the zero angular momentum observer frame (ZAMO frame, [Bardeen et al. 1972](#)), $u^{(\mu)} = e^{(\mu)}_\alpha u^\alpha$ is the four-velocity of the gas in the ZAMO frame, $e^\mu_{(\alpha)}$ is the inverse matrix of $e^{(\mu)}_\alpha$, and $d/d\tau = u^\mu \partial_\mu$ is the derivative of proper time, τ ([Mihalas & Mihalas 1984](#)). Now using equation (C5) and (C6), we get

$$\begin{aligned}
& w \left[e_{(\alpha)}^i - \frac{u^i}{u^t} e_{(\alpha)}^t \right] \frac{du^{(\alpha)}}{d\tau} \\
& = -w u^\mu \left[\partial_\mu \left\{ e_{(\alpha)}^i \right\} - \frac{u^i}{u^t} \partial_\mu \left\{ e_{(\alpha)}^t \right\} \right] u^{(\alpha)} \\
& \quad - \partial_\mu \left\{ (p_{\text{gas}} + p_{\text{mag}}) g^{\mu i} \right\} + \frac{u^i}{u^t} \partial_\mu \left\{ (p_{\text{gas}} + p_{\text{mag}}) g^{\mu t} \right\} \\
& \quad + \partial_\mu (b^i b^\mu) - \frac{u^i}{u^t} \partial_\mu (b^t b^\mu) \\
& \quad - \left(T^{\mu i} - \frac{u^i}{u^t} T^{\mu t} \right) \frac{\partial_\mu \sqrt{-g}}{\sqrt{-g}} \\
& \quad - \left(\Gamma_{\alpha\mu}^i - \frac{u^i}{u^t} \Gamma_{\alpha\mu}^t \right) T^{\alpha\mu} + G^i - \frac{u^i}{u^t} G^t.
\end{aligned} \tag{C7}$$

We calculate the equation of motion in the r -direction. In order to obtain a concrete expression, it is necessary to fix the space-time. We consider the Boyer-Lindquist metric with a spin parameter of zero. In this case, all nondiagonal

components of $e^{(\mu)}_{\alpha}$ are zero. Assuming steady ($\partial_t = 0$) and axisymmetric ($\partial_{\phi} = 0$) flow, the following equation of motion in the radial direction is obtained:

$$f_{\text{grav}}^{(r)} + f_{\text{thermal}}^{(r)} + f_{\theta,\text{cent}}^{(r)} + f_{\phi,\text{cent}}^{(r)} + f_{\text{rad}}^{(r)} + f_{\text{mag}}^{(r)} + f_{\text{adv}}^{(r)} = 0 \quad (\text{C8})$$

where $f_{\text{grav}}^{(r)}$, $f_{\text{thermal}}^{(r)}$, $f_{\theta,\text{cent}}^{(r)}$, $f_{\phi,\text{cent}}^{(r)}$, $f_{\text{rad}}^{(r)}$, $f_{\text{mag}}^{(r)}$, and $f_{\text{adv}}^{(r)}$ describe the gravitational force, thermal force, centrifugal force due to the poloidal motion, centrifugal force due to the toroidal motion, radiation force, Lorentz force, and advection force, respectively. These force can be described as follows:

$$f_{\text{grav}}^{(r)} = \frac{M_{\text{NS}}}{r^2} w (u^t u_t + u^r u_r), \quad (\text{C9})$$

$$f_{\text{thermal}}^{(r)} = - \left(1 - \frac{2M_{\text{NS}}}{r} \right) \partial_r p_{\text{gas}}, \quad (\text{C10})$$

$$f_{\theta,\text{cent}}^{(r)} = \left(1 - \frac{2M_{\text{NS}}}{r} \right) w \frac{u^{\theta} u_{\theta}}{r}, \quad (\text{C11})$$

$$f_{\phi,\text{cent}}^{(r)} = \left(1 - \frac{2M_{\text{NS}}}{r} \right) w \frac{u^{\phi} u_{\phi}}{r}, \quad (\text{C12})$$

$$f_{\text{rad}}^{(r)} = G^r - \frac{u^r}{u^t} G^t, \quad (\text{C13})$$

$$\begin{aligned} f_{\text{mag}}^{(r)} = & - \left(1 - \frac{2M_{\text{NS}}}{r} \right) \partial_r \left(\frac{b^2}{2} \right) \\ & + \partial_{\mu} (b^{\mu} b^r) - \frac{u^r}{u^t} \partial_{\mu} (b^{\mu} b^t) \\ & + \left(\frac{2b^r}{r} + \frac{b^{\theta}}{\tan \theta} \right) \left(b^r - \frac{u^r}{u^t} b^t \right) \\ & - \frac{M_{\text{NS}}}{r} \frac{b^t b_t + b^r b_r}{r} \\ & - \left(1 - \frac{2M_{\text{NS}}}{r} \right) \frac{b^{\theta} b_{\theta} + b^{\phi} b_{\phi}}{r} \\ & - \frac{2M_{\text{NS}}}{r^2} \frac{u^r}{u^t} b^t b_r, \end{aligned} \quad (\text{C14})$$

$$f_{\text{adv}}^{(r)} = -w\gamma \left(1 - \frac{2M_{\text{NS}}}{r} \right)^{1/2} (u^r \partial_r + u^{\theta} \partial_{\theta}) v^{(r)} \quad (\text{C15})$$

where $\gamma = u^{(t)}$ is the Lorentz factor in the ZAMO frame (i.e. statistic observer frame), and $v^{(r)} = u^{(r)}/r^{(t)}$. The equation of motion in the θ -direction can also be obtained by the same procedure.

$$f_{\text{inertial}}^{(\theta)} + f_{\text{thermal}}^{(\theta)} + f_{\phi,\text{cent}}^{(\theta)} + f_{\text{rad}}^{(\theta)} + f_{\text{mag}}^{(\theta)} + f_{\text{adv}}^{(\theta)} = 0, \quad (\text{C16})$$

where $f_{\text{inertial}}^{(\theta)}$ is the inertial force caused by the motion in the direction of θ . These force are written as follows:

$$f_{\text{inertial}}^{(\theta)} = -w u_r u^{\theta} \left(1 - \frac{3M_{\text{NS}}}{r} \right), \quad (\text{C17})$$

$$f_{\text{thermal}}^{(\theta)} = -\frac{1}{r} \partial_{\theta} p_{\text{gas}}, \quad (\text{C18})$$

$$f_{\phi,\text{cent}}^{(\theta)} = w \frac{u^{\phi} u_{\phi}}{r \tan \theta}, \quad (\text{C19})$$

$$f_{\text{rad}}^{(\theta)} = r \left(G^{\theta} - \frac{u^{\theta}}{u^t} G^t \right), \quad (\text{C20})$$

$$\begin{aligned} f_{\text{mag}}^{(\theta)} = & -\frac{1}{r} \partial_{\theta} \left(\frac{b^2}{2} \right) + r \partial_{\mu} (b^{\mu} b^{\theta}) \\ & - r \frac{u^{\theta}}{u^t} \partial_{\mu} (b^{\mu} b^t) + r \left(\frac{2b^r}{r} + \frac{b^{\theta}}{\tan \theta} \right) \left(b^{\theta} - \frac{u^{\theta}}{u^t} b^t \right) \end{aligned}$$

$$+ 2b^r b^\theta - \frac{b^\phi b_\phi}{r \tan \theta} - \frac{u^\theta}{u^t} \frac{2M}{r} b^t b_r, \quad (\text{C21})$$

$$f_{\text{adv}}^{(\theta)} = -w\gamma (u^r \partial_r + u^\theta \partial_\theta) v^{(\theta)}, \quad (\text{C22})$$

where $v^{(\theta)} = u^{(\theta)}/u^{(t)}$. The relativistic equations of motion derived by this method reduce to the Newtonian equations of motion for $\mathcal{O}((w - \rho)/\rho) \rightarrow 0$, $\mathcal{O}(v/c) \rightarrow 0$, and $\mathcal{O}(M/r) \rightarrow 0$.

REFERENCES

- Abarca, D., Parfrey, K., & Kluźniak, W. 2021, *ApJL*, 917, L31, doi: [10.3847/2041-8213/ac1859](https://doi.org/10.3847/2041-8213/ac1859)
- Abolmasov, P., & Lipunova, G. 2022, arXiv e-prints, arXiv:2207.12312, doi: [10.48550/arXiv.2207.12312](https://doi.org/10.48550/arXiv.2207.12312)
- Asahina, Y., & Ohsuga, K. 2022, *ApJ*, 929, 93, doi: [10.3847/1538-4357/ac5d37](https://doi.org/10.3847/1538-4357/ac5d37)
- Asahina, Y., Takahashi, H. R., & Ohsuga, K. 2020, *ApJ*, 901, 96, doi: [10.3847/1538-4357/abaf51](https://doi.org/10.3847/1538-4357/abaf51)
- Bachetti, M., Harrison, F. A., Walton, D. J., et al. 2014, *Nature*, 514, 202, doi: [10.1038/nature13791](https://doi.org/10.1038/nature13791)
- Bardeen, J. M., Press, W. H., & Teukolsky, S. A. 1972, *ApJ*, 178, 347, doi: [10.1086/151796](https://doi.org/10.1086/151796)
- Basko, M. M., & Sunyaev, R. A. 1976, *MNRAS*, 175, 395, doi: [10.1093/mnras/175.2.395](https://doi.org/10.1093/mnras/175.2.395)
- Belfiore, A., Esposito, P., Pintore, F., et al. 2020, *Nature Astronomy*, 4, 147, doi: [10.1038/s41550-019-0903-z10.48550/arXiv.1910.11876](https://doi.org/10.1038/s41550-019-0903-z10.48550/arXiv.1910.11876)
- Chashkina, A., Abolmasov, P., & Poutanen, J. 2017, *MNRAS*, 470, 2799, doi: [10.1093/mnras/stx1372](https://doi.org/10.1093/mnras/stx1372)
- Chashkina, A., Lipunova, G., Abolmasov, P., & Poutanen, J. 2019, *A&A*, 626, A18, doi: [10.1051/0004-6361/201834414](https://doi.org/10.1051/0004-6361/201834414)
- Chen, X., Wang, W., & Tong, H. 2021, *Journal of High Energy Astrophysics*, 31, 1, doi: [10.1016/j.jheap.2021.04.00210.48550/arXiv.2104.09076](https://doi.org/10.1016/j.jheap.2021.04.00210.48550/arXiv.2104.09076)
- Das, P., Porth, O., & Watts, A. L. 2022, *MNRAS*, 515, 3144, doi: [10.1093/mnras/stac1817](https://doi.org/10.1093/mnras/stac1817)
- Doroshenko, V., Tsygankov, S., & Santangelo, A. 2018, *A&A*, 613, A19, doi: [10.1051/0004-6361/20173220810.48550/arXiv.1710.10912](https://doi.org/10.1051/0004-6361/20173220810.48550/arXiv.1710.10912)
- Doroshenko, V., Zhang, S. N., Santangelo, A., et al. 2020, *MNRAS*, 491, 1857, doi: [10.1093/mnras/stz2879](https://doi.org/10.1093/mnras/stz2879)
- Fabrika, S. N., Atapin, K. E., Vinokurov, A. S., & Sholukhova, O. N. 2021, *Astrophysical Bulletin*, 76, 6, doi: [10.1134/S1990341321010077](https://doi.org/10.1134/S1990341321010077)
- Fishbone, L. G., & Moncrief, V. 1976, *ApJ*, 207, 962, doi: [10.1086/154565](https://doi.org/10.1086/154565)
- Fragile, P. C., Etheridge, S. M., Anninos, P., Mishra, B., & Kluźniak, W. 2018, *ApJ*, 857, 1, doi: [10.3847/1538-4357/aab788](https://doi.org/10.3847/1538-4357/aab788)
- Fürst, F., Walton, D. J., Harrison, F. A., et al. 2016, *ApJL*, 831, L14, doi: [10.3847/2041-8205/831/2/L14](https://doi.org/10.3847/2041-8205/831/2/L14)
- Illarionov, A. F., & Sunyaev, R. A. 1975, *A&A*, 39, 185
- Inoue, A., Ohsuga, K., & Kawashima, T. 2020, *PASJ*, 72, 34, doi: [10.1093/pasj/psaa010](https://doi.org/10.1093/pasj/psaa010)
- Israel, G. L., Belfiore, A., Stella, L., et al. 2017a, *Science*, 355, 817, doi: [10.1126/science.aai8635](https://doi.org/10.1126/science.aai8635)
- Israel, G. L., Papitto, A., Esposito, P., et al. 2017b, *MNRAS*, 466, L48, doi: [10.1093/mnrasl/slw218](https://doi.org/10.1093/mnrasl/slw218)
- Jaisawal, G. K., Wilson-Hodge, C. A., Fabian, A. C., et al. 2019, *ApJ*, 885, 18, doi: [10.3847/1538-4357/ab4595](https://doi.org/10.3847/1538-4357/ab4595)
- Jiang, Y.-F., Stone, J. M., & Davis, S. W. 2014, *ApJ*, 796, 106, doi: [10.1088/0004-637X/796/2/106](https://doi.org/10.1088/0004-637X/796/2/106)
- Kaaret, P., Feng, H., & Roberts, T. P. 2017, *ARA&A*, 55, 303, doi: [10.1146/annurev-astro-091916-055259](https://doi.org/10.1146/annurev-astro-091916-055259)
- Kanno, Y., Harada, T., & Hanawa, T. 2013, *PASJ*, 65, 72, doi: [10.1093/pasj/65.4.72](https://doi.org/10.1093/pasj/65.4.72)
- Kawashima, T., Mineshige, S., Ohsuga, K., & Ogawa, T. 2016, *PASJ*, 68, 83, doi: [10.1093/pasj/psw075](https://doi.org/10.1093/pasj/psw075)
- Kawashima, T., Ohsuga, K., Mineshige, S., et al. 2012, *ApJ*, 752, 18, doi: [10.1088/0004-637X/752/1/18](https://doi.org/10.1088/0004-637X/752/1/18)
- King, A., & Lasota, J.-P. 2019, *MNRAS*, 485, 3588, doi: [10.1093/mnras/stz720](https://doi.org/10.1093/mnras/stz720)
- Kitaki, T., Mineshige, S., Ohsuga, K., & Kawashima, T. 2017, *PASJ*, 69, 92, doi: [10.1093/pasj/psx101](https://doi.org/10.1093/pasj/psx101)
- . 2021, *PASJ*, 73, 450, doi: [10.1093/pasj/psab011](https://doi.org/10.1093/pasj/psab011)
- Kluźniak, W., & Lasota, J. P. 2015, *MNRAS*, 448, L43, doi: [10.1093/mnrasl/slu200](https://doi.org/10.1093/mnrasl/slu200)
- Kong, L.-D., Zhang, S., Zhang, S.-N., et al. 2022, *ApJL*, 933, L3, doi: [10.3847/2041-8213/ac7711](https://doi.org/10.3847/2041-8213/ac7711)
- Kosec, P., Pinto, C., Walton, D. J., et al. 2018, *MNRAS*, 479, 3978, doi: [10.1093/mnras/sty1626](https://doi.org/10.1093/mnras/sty1626)
- Kulkarni, A. K., & Romanova, M. M. 2008, *MNRAS*, 386, 673, doi: [10.1111/j.1365-2966.2008.13094.x](https://doi.org/10.1111/j.1365-2966.2008.13094.x)
- Levermore, C. D. 1984, *JQSRT*, 31, 149, doi: [10.1016/0022-4073\(84\)90112-2](https://doi.org/10.1016/0022-4073(84)90112-2)
- Lii, P. S., Romanova, M. M., Ustyugova, G. V., Koldoba, A. V., & Lovelace, R. V. E. 2014, *MNRAS*, 441, 86, doi: [10.1093/mnras/stu495](https://doi.org/10.1093/mnras/stu495)
- Long, M., Romanova, M. M., & Lovelace, R. V. E. 2007, *MNRAS*, 374, 436, doi: [10.1111/j.1365-2966.2006.11192.x](https://doi.org/10.1111/j.1365-2966.2006.11192.x)

- Lovelace, R. V. E., Romanova, M. M., & Bisnovatyi-Kogan, G. S. 1999, *ApJ*, 514, 368, doi: [10.1086/306945](https://doi.org/10.1086/306945)
- Makishima, K., Mihara, T., Nagase, F., & Tanaka, Y. 1999, *ApJ*, 525, 978, doi: [10.1086/307912](https://doi.org/10.1086/307912)
- Mihalas, D., & Mihalas, B. W. 1984, *Foundations of radiation hydrodynamics* (New York: Oxford Univ. Press)
- Mushtukov, A. A., Ingram, A., Middleton, M., Nagirner, D. I., & van der Klis, M. 2019, *MNRAS*, 484, 687, doi: [10.1093/mnras/sty3525](https://doi.org/10.1093/mnras/sty3525)
- Mushtukov, A. A., Suleimanov, V. F., Tsygankov, S. S., & Poutanen, J. 2015, *MNRAS*, 454, 2539, doi: [10.1093/mnras/stv2087](https://doi.org/10.1093/mnras/stv2087)
- Mushtukov, A. A., Verhagen, P. A., Tsygankov, S. S., et al. 2018, *MNRAS*, 474, 5425, doi: [10.1093/mnras/stx2905](https://doi.org/10.1093/mnras/stx2905)
- Narayan, R., Sądowski, A., & Soria, R. 2017, *MNRAS*, 469, 2997, doi: [10.1093/mnras/stx1027](https://doi.org/10.1093/mnras/stx1027)
- Narayan, R., & Yi, I. 1994, *ApJL*, 428, L13, doi: [10.1086/187381](https://doi.org/10.1086/187381)
- Ohsuga, K. 2007, *PASJ*, 59, 1033, doi: [10.1093/pasj/59.5.1033](https://doi.org/10.1093/pasj/59.5.1033)
- Ohsuga, K., & Takahashi, H. R. 2016, *ApJ*, 818, 162, doi: [10.3847/0004-637X/818/2/162](https://doi.org/10.3847/0004-637X/818/2/162)
- Pakull, M. W., & Grisé, F. 2008, in *American Institute of Physics Conference Series*, Vol. 1010, *A Population Explosion: The Nature & Evolution of X-ray Binaries in Diverse Environments*, ed. R. M. Bandyopadhyay, S. Wachter, D. Gelino, & C. R. Gelino, 303–307, doi: [10.1063/1.294506210.48550/arXiv.0803.4345](https://doi.org/10.1063/1.294506210.48550/arXiv.0803.4345)
- Parfrey, K., & Tchekhovskoy, A. 2017, *ApJL*, 851, L34, doi: [10.3847/2041-8213/aa9c85](https://doi.org/10.3847/2041-8213/aa9c85)
- Pinto, C., Middleton, M. J., & Fabian, A. C. 2016, *Nature*, 533, 64, doi: [10.1038/nature17417](https://doi.org/10.1038/nature17417)
- Poutanen, J., Lipunova, G., Fabrika, S., Butkevich, A. G., & Abolmasov, P. 2007, *MNRAS*, 377, 1187, doi: [10.1111/j.1365-2966.2007.11668.x](https://doi.org/10.1111/j.1365-2966.2007.11668.x)
- Qiu, Y., & Feng, H. 2021, *ApJ*, 906, 36, doi: [10.3847/1538-4357/abc95910.48550/arXiv.2011.05781](https://doi.org/10.3847/1538-4357/abc95910.48550/arXiv.2011.05781)
- Ratheesh, A., Dovčiak, M., Krawczynski, H., et al. 2023, *arXiv e-prints*, arXiv:2304.12752, doi: [10.48550/arXiv.2304.12752](https://doi.org/10.48550/arXiv.2304.12752)
- Romanova, M. M., Ustyugova, G. V., Koldoba, A. V., & Lovelace, R. V. E. 2011, *MNRAS*, 416, 416, doi: [10.1111/j.1365-2966.2011.19050.x](https://doi.org/10.1111/j.1365-2966.2011.19050.x)
- Romanova, M. M., Ustyugova, G. V., Koldoba, A. V., Wick, J. V., & Lovelace, R. V. E. 2003, *ApJ*, 595, 1009, doi: [10.1086/377514](https://doi.org/10.1086/377514)
- Sadowski, A., Lasota, J.-P., Abramowicz, M. A., & Narayan, R. 2016, *MNRAS*, 456, 3915, doi: [10.1093/mnras/stv285410.48550/arXiv.1510.08845](https://doi.org/10.1093/mnras/stv285410.48550/arXiv.1510.08845)
- Sadowski, A., Narayan, R., Tchekhovskoy, A., et al. 2015, *MNRAS*, 447, 49, doi: [10.1093/mnras/stu2387](https://doi.org/10.1093/mnras/stu2387)
- Sadowski, A., Narayan, R., Tchekhovskoy, A., & Zhu, Y. 2013, *MNRAS*, 429, 3533, doi: [10.1093/mnras/sts632](https://doi.org/10.1093/mnras/sts632)
- Sathyaprakash, R., Roberts, T. P., Walton, D. J., et al. 2019, *MNRAS*, 488, L35, doi: [10.1093/mnrasl/slz08610.48550/arXiv.1906.00640](https://doi.org/10.1093/mnrasl/slz08610.48550/arXiv.1906.00640)
- Shakura, N. I., & Sunyaev, R. A. 1973, *A&A*, 24, 337
- Shapiro, S. L., & Teukolsky, S. A. 1986, *Black Holes, White Dwarfs and Neutron Stars: The Physics of Compact Objects* (New York: Wiley-VCH)
- Takahashi, H. R., Mineshige, S., & Ohsuga, K. 2018, *ApJ*, 853, 45, doi: [10.3847/1538-4357/aaa082](https://doi.org/10.3847/1538-4357/aaa082)
- Takahashi, H. R., & Ohsuga, K. 2017, *ApJL*, 845, L9, doi: [10.3847/2041-8213/aa8222](https://doi.org/10.3847/2041-8213/aa8222)
- Takasao, S., Tomida, K., Iwasaki, K., & Suzuki, T. K. 2022, *ApJ*, 941, 73, doi: [10.3847/1538-4357/ac9eb1](https://doi.org/10.3847/1538-4357/ac9eb1)
- Tao, L., Feng, H., Zhang, S., et al. 2019, *ApJ*, 873, 19, doi: [10.3847/1538-4357/ab0211](https://doi.org/10.3847/1538-4357/ab0211)
- Thorne, K. S. 1981, *MNRAS*, 194, 439, doi: [10.1093/mnras/194.2.439](https://doi.org/10.1093/mnras/194.2.439)
- Tsygankov, S. S., Doroshenko, V., Mushtukov, A. A., Lutovinov, A. A., & Poutanen, J. 2018, *MNRAS*, 479, L134, doi: [10.1093/mnrasl/sly116](https://doi.org/10.1093/mnrasl/sly116)
- Urquhart, R., & Soria, R. 2016, *MNRAS*, 456, 1859, doi: [10.1093/mnras/stv2293](https://doi.org/10.1093/mnras/stv2293)
- Utsumi, A., Ohsuga, K., Takahashi, H. R., & Asahina, Y. 2022, *ApJ*, 935, 26, doi: [10.3847/1538-4357/ac7eb8](https://doi.org/10.3847/1538-4357/ac7eb8)
- van den Eijnden, J., Degenaar, N., Russell, T. D., et al. 2018, *Nature*, 562, 233, doi: [10.1038/s41586-018-0524-1](https://doi.org/10.1038/s41586-018-0524-1)
- van den Eijnden, J., Degenaar, N., Schulz, N. S., et al. 2019, *MNRAS*, 487, 4355, doi: [10.1093/mnras/stz1548](https://doi.org/10.1093/mnras/stz1548)
- Veledina, A., Muleri, F., Poutanen, J., et al. 2023, *arXiv e-prints*, arXiv:2303.01174, doi: [10.48550/arXiv.2303.01174](https://doi.org/10.48550/arXiv.2303.01174)
- Wasserman, I., & Shapiro, S. L. 1983, *ApJ*, 265, 1036, doi: [10.1086/160745](https://doi.org/10.1086/160745)
- Watarai, K.-y., & Fukue, J. 1999, *PASJ*, 51, 725, doi: [10.1093/pasj/51.5.725](https://doi.org/10.1093/pasj/51.5.725)
- Wijnands, R., Degenaar, N., & Page, D. 2017, *Journal of Astrophysics and Astronomy*, 38, 49, doi: [10.1007/s12036-017-9466-5](https://doi.org/10.1007/s12036-017-9466-5)
- Yoshioka, S., Mineshige, S., Ohsuga, K., Kawashima, T., & Kitaki, T. 2022, *PASJ*, 74, 1378, doi: [10.1093/pasj/psac076](https://doi.org/10.1093/pasj/psac076)
- Zhang, L., Blaes, O., & Jiang, Y.-F. 2022, *MNRAS*, 515, 4371, doi: [10.1093/mnras/stac1815](https://doi.org/10.1093/mnras/stac1815)